Geosci. Model Dev. Discuss., 4, 289–342, 2011
www.geosci-model-dev-discuss.net/4/289/2011/
doi:10.5194/gmdd-4-289-2011

Geoscientific Model Development Discussions

The role of phytoplankton dynamics in the seasonal variability of carbon in the subpolar North Atlantic – a modeling study

S. R. Signorini[1,9], S. Häkkinen[2], K. Gudmundsson[3], A. Olsen[4,5], A. M. Omar[4,5], J. Olafsson[6], G. Reverdin[7], S. A. Henson[8], and C. R. McClain[9]

[1]Science Applications International Corp., Beltsville, Maryland, USA
[2]NASA Goddard Space Flight Center, Cryospheric Sciences Branch, Greenbelt, Maryland, USA
[3]Marine Research Institute, P.O. Box 1390, 121 Reykjavik, Iceland
[4]Uni Bjerknes Centre, Allégaten 55, 5007 Bergen, Norway
[5]Bjerknes Centre for Climate Research, Allégaten 55, 5007 Bergen, Norway
[6]University of Iceland and Marine Research Institute, Reykjavik, Iceland
[7]Laboratoire d'Océanographie Dynamique et de Climatologie, IPSL, Boîte 100 – 4, Place Jussieu 75252, Paris, France

[8] National Oceanographic Centre, European Way, Southampton, SO14 3ZH, UK
[9] NASA Goddard Space Flight Center, Ocean Ecology Branch, Greenbelt, Code 614.2, Maryland, USA

Received: 3 January 2011 – Accepted: 16 January 2011 – Published: 4 February 2011

Correspondence to: S. R. Signorini (sergio.signorini@nasa.gov)

Published by Copernicus Publications on behalf of the European Geosciences Union.

Abstract

We use an ecosystem/biogeochemical model, which includes multiple phytoplankton functional groups and carbon cycle dynamics, to investigate physical-biological interactions in Icelandic waters. Satellite and in situ data were used to validate the model. The seasonality of the coccolithophore and "other phytoplankton" (diatoms and dinoflagellates) blooms is in general agreement with satellite ocean color products. Nutrient supply, biomass and calcite concentrations are modulated by light and mixed layer depth seasonal cycles. Diatoms are the most abundant with a large bloom in early spring and a secondary bloom in fall. The diatom bloom is followed by blooms of dinoflagellates and coccolithophores. The effect of biological changes on the seasonal variability of the surface ocean pCO_2 is nearly twice the temperature effect. The inclusion of multiple functional groups in the model played a major role in the accurate representation of CO_2 uptake by biology. For instance, at the peak of the bloom, the exclusion of coccolithophores causes an increase in alkalinity of up to 4 µmol kg^{-1} with a corresponding increase in DIC of up to 16 µmol kg^{-1}. The net effect of the absence of the coccolithophores bloom is an increase in pCO_2 of more than 20 µatm and a reduction of atmospheric CO_2 uptake of more than 6 mmol m^{-2} d^{-1}.

1 Introduction

The waters surrounding Iceland are characterized by the cold Polar water of the East Greenland Current and Arctic water of the East Icelandic Current from the north, and the warm North Atlantic water of the Irminger Current from the south (Gudmundsson, 1998). Figure 1 shows a map containing the Subpolar North Atlantic and Nordic Seas and the annual climatologic (1948–2009) surface currents and the mean location of the Arctic Front (AF) derived from the three-dimensional (3-D) coupled ice-ocean model of the Arctic and North Atlantic (Sirpa Häkkinen, personal communication, 2010; Hakkinen, 1995; Hakkinen and Proshutinsky, 2004), which is used in this study to

GMDD
4, 289–342, 2011

provide physical forcing for the 1-D ecosystem/carbon model (black triangle in Fig. 1 at 30° W, 60° N). The 1-D model location lies on the western edge of the Reykjanes Ridge and within the Irminger Current, in an area where winter mixing is extremely vigorous (mixed layer depths approaching 600 m) (Bailey et al., 2005) and spring-summer phytoplankton blooms are substantial (Fernandez et al., 1993; Holligan et al., 1993a; Weeks et al., 1993). The convergence of the Polar and North Atlantic water masses form the AF, which varies slightly in location seasonally (Fig. 2) and is identified by strong gradients of surface temperature (SST) and salinity (SSS). The AF runs east-west approximately along 66° N to the west of Iceland, and north-south between 12° W–8° W, and then further in northerly direction from approximately 69° N, northeast of Iceland. The above features are clearly shown in Fig. 2, which shows the seasonal SST and SSS fields for 2005 obtained from the 3-D coupled ice-ocean model of the Arctic and North Atlantic (Sirpa Häkkinen, personal communication; Hakkinen, 1995; Hakkinen and Proshutinsky, 2004). Model products are available at monthly intervals for the 1948–2009. We chose to show fields for 2005 as an example because it coincides with the year during which most of the surface ocean pCO_2 data are available (Chierici et al., 2009; Olsen et al., 2008). The 3-D model surface current vectors are superimposed on the SST and SSS fields, and show a complex circulation with swift currents and convergent/divergent regions that drive the strong horizontal SST and SSS gradients. The circulation pattern shown in Fig. 1 is consistent with previous descriptions of the regional circulation (Gudmundsson, 1998; Poulain et al., 1996). Sea ice is present throughout the year along the east coast of Greenland, with the ice edge extending farthest offshore in winter-spring, and retreating in the fall. Ice melt in summer-fall freshens (32–34 psu) the surface waters north of the AF. South of the AF waters are saltier (~35 psu) and warmer (8 to 12 °C) as a result of Atlantic Water intrusions. These hydrographic characteristics are reflected in the 3-D model mixed layer depth (MLD) seasonally (not shown). During winter and spring, MLDs average 100 to 500 m south of the AF, with deeper values in the Irminger and Icelandic Basins. In summer, the vertical stratification is significant with MLDs less than 20 m. North of the AF the MLDs are

GMDD
4, 289–342, 2011

shallow (<40 m) throughout the year due to the southward advection of fresher Polar and Arctic waters, and ice melting during summer–fall.

These large seasonal changes in stratification and vertical mixing play an important role in the euphotic zone nutrient renewal and on the onset and duration of the phytoplankton spring bloom (Henson et al., 2006; Holliday et al., 2006; Waniek et al., 2006). Variability in the intensity of primary production in general, and of the timing of spring bloom in particular (Henson et al., 2009), affects the population dynamics of higher trophic levels, such as the commercially important atlanto-scandian herring (Jakobsson, 1978) in the region. Phytoplankton primary production in Icelandic waters is large; the average of measurements during May–June range from 4.3 to 9.2 mg C m^{-3} h^{-1} for the different regions north and south of Iceland, respectively (Gudmundsson, 1998). In addition, seasonal and interannual changes in phytoplankton production are tightly coupled to atmospheric CO_2 uptake and surface ocean pCO_2 variability, and therefore a major component of the carbon cycle.

Coupled biogeochemical-physical numerical models together with observations are an essential tool to understand the interaction between physical and biological processes and the control processes creating the observed variability over a wide range of time scales ranging from days to years. Here we provide a description of a coupled biogeochemical-physical model which includes multiple phytoplankton functional groups and carbon cycle dynamics, with an application in Icelandic waters. The rationale for the site selection relates to a combination of environmental and biological factors, e.g., large range in MLD, low mean horizontal advection, clear seasonal succession of phytoplankton species, and bloom intensity.

GMDD
4, 289–342, 2011

2 Data sources and methodology

2.1 Satellite and in situ data sets

We rely on a combination of satellite data and field observations to provide a validation framework for the model. The satellite-derived data sets consist of SeaWiFS and MODIS Chl-*a*, MODIS and Reynolds and Smith optimally interpolated (RSOI) SST (Reynolds and Smith, 1995), and primary production from the Carbon-based Productivity Model (CbPM, Behrenfeld et al., 2005). Both empirical (OC4v4, OC3) and semi-analytical derived Chl-*a* products (MEaSUREs) were used to validate the model. The MEaSURES semi-analytical Chl-*a* product uses the Garver-Siegel-Maritorena (GSM) algorithm (Maritorena et al., 2002) available from the web site ftp://ftp.oceancolor.ucsb.edu//pub/org/oceancolor/MEaSUREs/.

The satellite-derived PP data were obtained from the Ocean Productivity web site at Oregon State University (http://www.science.oregonstate.edu/ocean.productivity/). In addition, a limited number of in situ PP data were obtained from C-14 incubations conducted during early August 2002 on a Marine Productivity (MarProd) cruise sponsored by the Natural Environment Research Council (UK) onboard the RRS Discovery, and we also use in situ primary production data from multi-year surveys in Icelandic waters, collated at the Marine Research Institute in Reykjavik.

Taxonomic data (cell counts) were obtained from the Continuous Plankton Recorder (CPR) database (standard area B6 south of Iceland, http://www.sahfos.ac.uk/data-archive/standard-areas.aspx).

Surface ocean pCO_2 data for 2005 were acquired from onboard the container ship M/V Nuka Arctica (Chierici et al., 2009; Olsen et al., 2008). In addition we have used DIC, alkalinity, surface ocean pCO_2, and nutrient in situ data from SURATLANTE (Corbiere et al., 2007; Metzl et al., 2010), and data from the CARbon IN the Atlantic Ocean (CARINA) Data Synthesis Project (Key et al., 2010).

GMDD
4, 289–342, 2011

The locations of all in situ data used to validate the 1-D ecosystem model are shown in Fig. 3. The atmospheric pCO_2 required to obtain the CO_2 flux at the atmosphere-ocean interface was obtained from GLOBALVIEW-CO_2 (NOAA, ftp://ftp.cmdl.noaa.gov).

2.2 One-dimensional model background

The mixed-layer/ecosystem model consists of a turbulence closure mixed layer model (TCMLM) coupled to the biogeochemical conservation equations. The mixed layer component originates from an existing one dimensional physical-biogeochemical model (Signorini et al., 2001a,b), hereafter referred to as ECO1D, that utilizes a turbulence closure mixed layer scheme (Mellor and Yamada, 1982). The TCMLM has a vertical coordinate system that provides parameter values, including horizontal velocity components, temperature, salinity, and the vertical diffusivity coefficient, k_v, at each time step and grid point. The surface boundary layer is resolved more accurately by using a stretched vertical coordinate with higher resolution near the surface.

The biogeochemical model is an upgraded version of the Signorini et al. (2003) model, which includes additional conservation equations for diatoms, coccolithophores, calcite ($CaCO_3$), silicate (SiO_2) and alkalinity. Formulations for $CaCO_3$ conservation equations follow those of the PISCES model (Aumont and Bopp, 2006). Figure 4 shows a diagram illustrating the model components and their couplings. The details of the ecosystem model are described in the Appendix A.

2.3 Model configuration and forcing

Figure 5 shows the satellite-derived net primary production (NPP) and calcification rate (P_{CaCO_3}) for June 1998, during which the strongest coccolithophore bloom has occurred during the SeaWiFS mission (Raitsos et al., 2006), with the location of the modeling site (black triangle at 30° W, 60° N). NPP was obtained from monthly CbPM files from the Ocean Productivity Oregon State web site (http://www.science.oregonstate.edu/

GMDD
4, 289–342, 2011

ocean.productivity/index.php), and the P_{CaCO_3} monthly composite was computed using the algorithm of Balch et al. (2007). The site lies at the western edge of the Reykjanes Ridge in the Irminger Sea, a region of high phytoplankton productivity. The local depth is ~1500 m but the model vertical grid extends to 1000 m only, which accommodates the deepest winter mixed layer depth (MLD). The TCMLM is forced by winds and other relevant atmospheric parameters to calculate heat and freshwater fluxes originating from NCEP-II Reanalysis products, which determined the 28-year period of simulation (1981–2008). The TCMLM is configured on a vertically-stretched logarithmic grid, while ECO1D uses a uniform vertical grid with 1 m resolution. Nutrient values below the mixed layer are nudged within the bounds of the observed monthly climatology from the World Ocean Atlas 2005 (see details in Appendix A), and deep water ($z > 500$ m) temperature and salinity values are nudged to values derived from the 3-D ice-ocean model using the Newtonian relaxation method (see Appendix A for details). The Newtonian relaxation method (nudging) is a simple form of data assimilation. Surface salinity (SSS) from the 3-D model is imposed at the top layer of the 1-D model, which accounts for all processes that alter SSS, including ice melting-freezing and precipitation-evaporation. The RSOI SST is imposed at the model surface instead of heat flux.

Deep water ($z > 200$ m) dissolved inorganic carbon (DIC) is nudged (relaxation time of 2 days) to values obtained from a data-derived equation (DIC vs. T) and model temperature at each time step (0.5 h), plus a superimposed DIC decadal trend consistent with observations (Signorini et al., 2011). The total alkalinity (TA) is nudged to values also obtained from a data-derived equation (TA vs. T and S) for depths greater than 200 m with a relaxation time scale of 10 days. The DIC and TA equations are based on CARINA observations with details described in the Appendix A.

GMDD
4, 289–342, 2011

2.4 Calculation of daily integrated primary production from field observations

For the integration of daily primary production (PP; mg C m^{-2} d^{-1}) we used interpolated depth distribution of Chl-*a* measured from water samples, and the photosynthetic response to light according to P-I experiments. The photosynthetically active radiation at the surface (PAR; W m^{-2}) was calculated, using the ratio 0.46 of global radiation according to the Frouin model (Frouin et al., 1989) and further modified by cloud cover according to analysis from NOAA NCEP-II. The light extinction with depth was calculated as function of Chl-*a* absorption and water depth.

The data, collated for offshore stations southwest of Iceland, was integrated for each meter depth (z) from surface to the bottom of the euphotic zone (Zeu) and 30-min intervals. The calculated photosynthetic response to PAR is integrated for the first 12 h of the day and then doubled, assuming symmetric distribution of PAR and the photosynthetic response. The integrated PP is calculated according to (Eq. B1) in Appendix B.

In order to compensate for effects of euphotic zone depth variations relative to surface mixed layer depths on the PP, we used a theoretical model (Appendix B) to modify the available light. Thus PP is a depth integrated daily carbon assimilation for the water column, modified with respect to both Zeu and MLD.

The incubation techniques used for measurements of photosynthesis and the P-I experiments do not account for fluctuations in light intensities. Nevertheless, it is well known that persistent exposure of phytoplankton to high light intensity during incubation in bottles may cause some, if not all, of the apparent and debated photoinhibition (Behrenfeld, 2002; Gallegos and Platt, 1985). The application of the tanh saturation (Eq. 1) ignores the inhibition of photosynthesis at high light intensities, as well as eventual reduction due to UV radiation.

GMDD
4, 289–342, 2011

3 Discussion

3.1 Ecosystem-carbon model validation

Using the data sets shown in Fig. 3 and discussed in Sects. 2.4, model versus data comparisons were compiled and analyzed. Due to the nature of the spatial distribution of the in situ data surrounding the model location, it is expected that some of the mismatches between model and observations are inherently related to the spatial variability and patchiness of measured quantities. For instance, the patchiness of primary production and calcite production can be readily seen in the satellite maps shown in Fig. 5. However, in spite of this spatial mismatch between the model single point simulation and available measurements in multiple locations around the model site, with few exceptions, the overall agreement between model and observations is quite good.

Figure 6a, b, and d show the seasonal cycles (2003–2008) of model Chl-*a* and MODIS Aqua OC3 and GSM Chl-*a* products, model and MODIS Aqua calcite concentration, and model partitioning of phytoplankton functional groups (diatoms, dinoflagellates, and coccolithophores), respectively. The aggregated, monthly averaged, phytoplankton group CPR data (cell counts) from standard area B6 south of Iceland are shown in Fig. 6c for comparison. The size of standard area B6 is relatively large (59° N to 64° N; 19° W to 31° W) so some spatial smoothing is to be expected. The model shows (Fig. 6d) that diatoms are the most abundant functional group with a large bloom in early spring and a secondary bloom in fall. The diatom bloom is followed by blooms of dinoflagellates and coccolithophores. The double diatom peak is also present in the CPR data (Fig. 6c). The abundance of coccolithophores is much smaller in the CPR data when compared to the model. However, the CPR mesh is large (250 µm) and therefore coccolithophores may not be representatively sampled. Previous field work studies in the Northeast North Atlantic report large concentrations of coccolithophores during the summer bloom. For example, Fernandez et al. (1993) report total estimated coccolithophore C biomass as large as 50% of the total phytoplankton C biomass.

GMDD
4, 289–342, 2011

The seasonal cycle of model Chl-*a* agrees well with both MODIS OC3 and GSM products, with peak values closer to the GSM Chl-*a*, quite possibly an indication of chromophoric dissolved organic matter (CDOM) influence (Nelson et al., 2007) on the empirical Chl-*a* product (OC3). The MODIS and model calcite concentration seasonal cycles start rising (growth phase) in April-May with peaks in June and August, respectively, with a decay phase thereafter. Although the peak value of model calcite is in agreement with MODIS, there is a 2-month phase shift between the model (August) and MODIS (June) maximum concentrations. A time series of model PP for which in situ measurements are available is shown in Fig. 7. Figure 7 also shows the monthly SeaWiFS-derived PP estimates from CbPM, the MLD, and the euphotic depth (Zeu). Note that the most productive periods of the bloom (when Zeu is shallowest) occur every year during highly stratified conditions (shallowest MLDs), an indication that light availability for photosynthesis is a major limiting factor on the seasonal variability of phytoplankton species in the region.

A more quantitative approach based on metrics, assessment indices and skill scores is provided to evaluate model performance. For this purpose, we use a Taylor diagram (Jolliff et al., 2009) to conduct the model evaluation based on all available in situ and satellite observations. The normalized standard deviation (σ^*) and the correlation coefficient (R) from the model (m) to reference field (r) comparisons may be displayed on a single Taylor diagram (Fig. 8). The Taylor diagram is a polar coordinate diagram that assigns the angular position to the inverse cosine of R ($\cos^{-1}(R)$). A correlation of zero is thus 90° away from a correlation of 1 (see scaling on Fig. 8). The radial (along-axis) distance from the origin is assigned to the normalized standard deviation. The reference field point (black circle in Fig. 8), which is comprised of the statistics generated from a redundant reference to reference comparison, is indicated for the polar coordinate (1.0, 0.0). The model to reference comparison points may then be gauged by how close they fall to the reference point. This distance is proportional to the normalized unbiased Root-Mean-Square Difference, as defined by the equation $\mathrm{RMSD}^{*'} = (1.0 + \sigma^{*2} - 2\sigma^* R)^{0.5}$, where $\sigma^* = \sigma_m/\sigma_r$.

GMDD
4, 289–342, 2011

Inspection of Fig. 8 reveals that the great majority of model versus reference comparisons fall within significant R values (0.7–0.9) and σ^* close to 1. All R-values are significant at the 95% confidence level, with p-values well below 0.05, with the exception of model-versus in situ PP which has a p-value of 0.582. The alkalinity reference has a relative low correlation with the model, even though the bias between model and observations is small. The Taylor diagram does not provide an estimate for the bias, but Table 1 provides surface ocean means and standard deviations (STDs) for all the variables shown in the Taylor diagram. With the exception of the in situ vs. model PP, the means and STDs for the model variables are very close to the observed values.

Despite having significant R values, the model has much larger nitrate σ than the observed reference. Time series of observed and model nutrients (not shown) reveal that the model underestimates all nutrients during 2005–2006, especially nitrate. However, the low winter nutrients are consistent with warmer winter SSTs, as given by both model and observations, and consequently shallower MLDs. Since these are the only two years during which the model underestimates nutrients, it is concluded that physical mechanisms other than vertical mixing, such as horizontal advection not captured by the 1-D dynamics, may have influenced winter nutrient renewal during that time.

Surface ocean pCO_2 references are in good agreement with the model ($R \sim 0.7$ and $\sigma^* \sim 1.0$). Finally, the model PP provides good agreement with the PP estimates derived with satellite-based CbPM using SeaWiFS data at the precise location of the model simulation. On the other hand, the in situ PP is, previously stated, in poor agreement with the model. This may be explained in part by the large spatial variability of PP around the model site (Fig. 5) and the scattered nature of the PP measurement locations (Fig. 3), as well as poor seasonal coverage. An error analysis of the log-transformed relative percent differences (RPDs) as a function of distance from the model site (60° N, 30° W) reveals the patchy nature of the PP field. The distances between model site and PP measurement location range from 48 to 568 km. The RPDs are within ±10% for distances less than 150 km, while the RPDs become much larger (up to 50%) for distances within the range of 150 to 320 km. The RPDs are significantly

GMDD
4, 289–342, 2011

reduced (±10%) again within the distance of 320 to 480 km and back to 50% for the most distant PP station locations (480 to 568 km).

3.2 Biogeochemical response to physical forcing

The seasonal changes in biogeochemical properties as a result of physical forcing are given in Fig. 9, which shows the model seasonal cycles of chlorophyll, calcite (PIC), SST, PAR, the ratio of euphotic depth to MLD (Zeu/MLD), and nutrients (NO_3, PO_4, and SiO_2). The rise of Chl-*a* starts in April when the Zeu/MLD ratio is ~0.5 and drawdown of nutrients ensues. The PIC concentration starts to rise in May when the Zeu/MLD ratio reaches ~2.0, an indication that the calcite-forming coccolithophores require much more light than the other phytoplankton to initiate the bloom. A broad peak in the total Chl-*a* from all three functional groups extends from May to September associated with shallower MLDs (Zeu/MLD ratio > 2.0). Depletion of light, nutrients, and grazing pressure reduces biomass significantly after September. The coccolithophore bloom, indicated by the changes in PIC concentration due to calcite production, peaks in July-August when light conditions (Zeu/MLD ratio > 4.0) provide favorable conditions for the bloom-forming coccolithophore *Emiliania huxleyi*, a species well known to the area (Holligan et al., 1993a,b; Fernandez et al., 1993; Balch et al., 1992). As the MLD deepens, and light (PAR) levels are significantly reduced, Chl-*a* and PIC concentrations drop gradually after September. This interplay of light availability, vigorous winter mixing/summer restratification, and nutrient availability is central to the classical North Atlantic spring bloom.

Time series of model profiles of temperature, nutrients, phytoplankton biomass, and primary production for 1981–2008 are shown in Figs. 10 and 11. All these parameters show significant interannual variability driven by changes in physical and biological forcing. For instance, Fig. 10 shows that nutrients respond to variations in vertical mixing caused by changes in the temperature vertical stratification. The white line superposed on temperature is the mean winter (DJFM) SST anomaly, which exhibits significant interannual changes, most prominent after 1996 when the winter anomalies

GMDD
4, 289–342, 2011

become positive with a visible trend. During this period there is a decline in nutrient concentrations resulting from a reduction in vertical mixing, primarily in the upper 400 m but more pronounced near the surface in summer when the biological demand is at its peak. Significant interannual changes are also observed in the phytoplankton biomass and primary production. Figure 11 shows the distinct seasonal cycles and interannual variability of biomass for diatoms, dinoflagellates, and coccolithophores, and the combined primary production for all three functional groups. The superposed lines on the vertical distribution of PP are the annual vertically integrated PP (solid line) and net community production (dashed line, N_P). There are some changes in PP and N_P before and after 1996. The average values of PP and N_P for the period 1981–1995 are 73.4 ± 78.5 and $49.5 \pm 54.2\,\mathrm{g\,C\,m^{-2}\,yr^{-1}}$, with a corresponding regenerated production of $23.9 \pm 26.2\,\mathrm{g\,C\,m^{-2}\,yr^{-1}}$. For the period of 1996–2008 the PP, N_P, and regenerated production are 77.8 ± 81.6, 48.4 ± 50.4, and $29.4 \pm 36.8\,\mathrm{g\,C\,m^{-2}\,yr^{-1}}$. So, on average, the PP increased for the period after 1996, while N_P decreased. These changes are not very large and not statistically different. They reflect the impact of interannual variations in vertical stratification and light and nutrient availability rather than measurable decadal trends.

3.3 Impact of phytoplankton blooms on carbon uptake

To better understand the impact of the phytoplankton blooms, including calcite-producing coccolithophore blooms, on the atmospheric carbon uptake, we need first review the thermodynamics of the CO_2 system before we analyze its impact on the upper ocean ecosystem-carbon interaction. Changes in surface ocean alkalinity and DIC due to physical-biogeochemical interactions are the main drivers for the surface ocean pCO_2 and, therefore air-sea CO_2 flux. The equations for TA and DIC are:

$$\mathrm{DIC} = \mathrm{CO_{2(aq)}} + [\mathrm{H_2CO_3}] + [\mathrm{HCO_3^-}] + [\mathrm{CO_3^{2-}}]$$

$$\mathrm{TA} = [\mathrm{HCO_3^-}] + 2[\mathrm{CO_3^{2-}}] + [\mathrm{OH^-}] - [\mathrm{H^+}] + [\mathrm{B(OH)_4^-}] + [\mathrm{H_3SiO_4^-}] + [\mathrm{HPO_4^{2-}}]$$

GMDD
4, 289–342, 2011

$$+2\left[PO_4^{3-}\right]-\left[HSO_4^-\right]-[HF]-\left[H_3PO_4\right] \quad (1)$$

where all quantities in brackets are stoichiometric concentrations. The first four terms in the TA equation are the major ones. $CO_{2(aq)}$ is the dissolved carbon dioxide, $[H_2CO_3]$ is the carbonic acid, $[HCO_3^-]$ is the bicarbonate ion, $[CO_3^{2-}]$ is the carbonate ion, and $[OH^-]$ and $[H^+]$ are the products of H_2O dissociation.

By photosynthesis in the photic zone, phytoplankton (in this model study diatoms, dinoflagellates, and coccolithophores) draws down CO_2:

$$16CO_2+16NO_3^-+H_2PO_4^-+17H^++122H_2O \leftrightarrow (CH_2O)_{106}(NH_3)_{16}H_3PO_4+138O_2 \quad (2)$$

In contrast, biogenic calcification (in this model study due to coccolithophores) releases CO_2:

$$Ca^{2+}+2HCO_3^- \rightarrow CaCO_3+CO_2+H_2O \quad (3)$$

Thus, the biological carbon pump can remove particulate carbon from the euphotic zone by exporting it to the ocean interior. Ballast minerals, such as the biogenic calcite ($CaCO_3$) enhance the flux of organic carbon from the surface ocean to the ocean floor (Koeve, 2002; Armstrong et al., 2002; Francois et al., 2002; Klaas and Archer, 2002). Counteraction of that is due to the dissolution of calcite that occurs below the calcite saturation horizon as it sinks down to the ocean floor. However, dissolution is not included and does not occur near the model site south of Iceland as the whole water column (at least down to 1000 m in the model) is currently above the calcite saturation level (Feely et al., 2004; Gehlen et al., 2007; Chung et al., 2003), and it is assumed that all ballast calcite that sinks from the euphotic zone will eventually reach the ocean bottom with minimal dissolution. The rain ratio, defined as the ratio of particulate inorganic carbon (PIC) to particulate organic carbon (POC) in exported biogenic matter, determines the relative strength of the biological carbon pump and consequently the flux of CO_2 across the surface ocean-atmosphere interface.

GMDD
4, 289–342, 2011

Inspection of Eqs. (1), (2), and (3) reveals some important interactions among factors related to photosynthesis, calcification, DIC and TA. These interactions are accounted for by the model as shown in Eqs. (A13) through (A17) in Appendix A, which calculate calcite detritus, calcite concentration, total CO_2, and alkalinity (det_{CaCO_3}, $CaCO_3$, DIC, and TA). Some notable interactions can be deduced from Eqs. (1)–(3). For instance, Eqs. (1) and (2) show that 1 mol of H^+ is consumed for each mole of NO_3^- or $H_2PO_4^-$ consumed through biosynthesis, increasing TA by 1 mol. On the other hand, for each mole of CO_2 consumed by biosynthesis, DIC decreases by 1 mol. These transformations are accounted for in the model's TA and DIC equations by the term *Np*, which is the net community production. Finally, the process of calcification ($CaCO_3$ production) shown in Eq. (3) implies that for each mole of $CaCO_3$ produced by the coccolithophores, TA decreases by 2 mol (−2 mol of HCO_3^- in Eq. 1) and DIC by 1 mol (−2 mol of HCO_3^- + 1 mol of CO_2 in Eq. 1).

In view of the complexity of these interactions, it is very difficult to separate in the model the individual effects of the phytoplankton groups on the carbon uptake. Instead, to address this issue we conducted a model experiment with the coccolithophore components turned off (no carbonate pump) and compared the results with the baseline experiment (biological and carbonate pumps) including all three functional groups (diatoms, dinoflagellates, and coccolithophores). The results are shown in Figs. 12 and 13 as seasonal 8-day climatologic averages for 1998–2008. In Fig. 12 we see the results of seasonal changes in the upper 120 m vertically-integrated phytoplankton biomass concentrations with and without the presence of coccolithophores (Fig. 12a and b, respectively), and the corresponding changes in net community production (Fig. 12c). In the presence of coccolithophores the yearly averaged integrated biomass for diatoms, dinoflagellates, and coccolithophores was 534, 318, and 184 mg C m^{-1}, respectively. The corresponding *Np* with all three functional groups was 134 mg C m^{-2} d^{-1}. With the exclusion of coccolithophores, the population of diatoms increased to an integrated value of 613 mg C m^{-2} and dinoflagellates to 341 mg C m^{-2}, respectively. However, there was a net decrease in *Np* to 104 mg C m^{-2} d^{-1}. The 22.4% reduction in *Np* has

GMDD
4, 289–342, 2011

consequences in the biological uptake of carbon. Figure 13 shows that, without the calcite production by coccolithophores, at the peak of the biological drawdown, the alkalinity (Fig. 13a) increases by up to 4 µmol kg^{-1} with a corresponding increase in DIC (Fig. 13b) of up to 16 µmol kg^{-1}. As a result, the net effect of the absence of the coccolithophores bloom is an increase in pCO_2 of more than 20 µatm (Fig 13c). The seasonal changes in the sea-air CO_2 flux are shown in Fig. 13d. At the peak of the bloom, the exclusion of coccolithophores causes a reduction of CO_2 uptake of more than 6 mmol m^{-2} d^{-1}. This result highlights the importance of including all major functional groups in the modeling of carbon variability in the subpolar North Atlantic.

The seasonal drawdown of surface ocean pCO_2 is a result of two competing effects, e.g., temperature warming and biological uptake effects. Takahashi et al. (2002) developed a method to separate these two effects for the global oceans. The effect of biology (B_e) on the surface ocean pCO_2 in a given area is represented by the seasonal amplitude of pCO_2 corrected to the mean annual temperature in that area. The effect of temperature changes (T_e) on the seasonal pCO_2 variations is represented by the seasonal amplitude of the mean annual pCO_2 corrected to the range of observed temperatures.

$$B_e = (\Delta pCO_2)_{bio} = (pCO_2 \text{ at } T_{mean})_{max} - (pCO_2 \text{ at } T_{mean})_{min}$$
$$T_e = (\Delta pCO_2)_{temp} = (pCO_2 \text{ at } T_{obs})_{max} - (pCO_2 \text{ at } T_{obs})_{min} \quad (4)$$

where the subscripts "min" and "max" indicate the seasonal minimum and maximum values. The relative importance of the biology and temperature effects can then be expressed by the ratio B_e/T_e. Using climatologic (1981–2008) model seasonal surface ocean pCO_2 and SST we calculate the ratio B_e/T_e as 1.92, which means that the biology effect is nearly twice the temperature effect in the shaping of the seasonal pCO_2 variability at the model location.

GMDD
4, 289–342, 2011

4 Summary and conclusions

Using a Taylor diagram, skill assessment of model versus field measurements reveals high scores for the majority of biogeochemical parameters for which in situ data are available.

The seasonal patterns of phytoplankton concentrations are a response to the interplay between light availability, vigorous winter mixing/summer restratification, and nutrient availability, not unlike the classical North Atlantic spring bloom. Functional groups compete seasonally for ideal growth conditions. Model results indicate that the spring-summer bloom consists predominantly of diatoms, with still significant but less intense blooms of dinoflagellates and coccolithophores. The model shows that the diatom biomass peaks in May with a secondary and less intense bloom in September. The dinoflagellates and coccolithophores peak in July through August during which drawdown of surface-ocean CO_2 reaches its maximum value. The effect of biological changes in the surface ocean pCO_2 exceeds the temperature effect by a factor of almost 2, a clear indication of the importance of phytoplankton photosynthesis on the uptake of atmospheric CO_2 in the region.

Model experiments were conducted to investigate the seasonal changes in phytoplankton concentration with and without the presence of coccolithophores, and their impact on carbon uptake. Without the influence of coccolithophore blooms, the alkalinity increases by almost 4 $\mu mol\,kg^{-1}$ and DIC is elevated by up to 16 $\mu mol\,kg^{-1}$. The net effect of coccolithophores blooms is an increase in pCO_2 of up to about 20 µatm during summer with a corresponding reduction of atmospheric CO_2 uptake of about 6 $mmol\,m^{-2}\,d^{-1}$, an indication of the importance of including all major phytoplankton functional groups when modeling the carbon variability in the subpolar North Atlantic.

GMDD
4, 289–342, 2011

Appendix A

Biogeochemical model description

The model features multiple functional groups (diatoms, dinoflagellates, and coccolithophores), zooplankton, nutrients (NO_3, PO_4, NH_4, SiO_2, and Fe), POC, DIC, DOC, alkalinity (TA), calcite production, chlorophyll, complete carbonate chemistry, and air-sea CO_2 flux. The governing equations for the biogeochemical model are provided hereafter, where the subscripted index $i = 1, 2, 3$ represent diatoms, dinoflagellates, and coccolithophores, respectively. Iron (Fe) limitation, although included in the model, was not considered in this study. However, there is evidence (Nielsdóttir et al., 2009) of iron limitation of the post-bloom (July to early September) phytoplankton communities in the Iceland Basin, east of the model location, where high nutrient-low chlorophyll (HNLC) conditions may occur. Iron limitation studies in the Iceland Basin will be a topic of future studies using the same model.

Phytoplankton (diatoms, dinoflagellates, and coccolithophores)

$$\frac{\partial P_i}{\partial t} + w\frac{\partial P_i}{\partial z} - \frac{\partial}{\partial z}\left[k_v \frac{\partial P_i}{\partial z}\right] = \mu_{i,\mathrm{phy}} P_i - \mu_{i,\mathrm{zoo}} Z - R_{\mathrm{phy,NO_3}}(P_i - P_{i.o}) - M_{\mathrm{phy,det}}(P_i - P_{i,o}) - w_{P_i}\frac{\partial P_i}{\partial z} \quad \text{(A1)}$$

Zooplankton

$$\frac{\partial Z}{\partial t} + w\frac{\partial Z}{\partial z} - \frac{\partial}{\partial z}\left[k_v \frac{\partial Z}{\partial z}\right] = \gamma \sum_i (\mu_{i,\mathrm{zoo}} Z) - E_{\mathrm{zoo,NO_3}}(Z - Z_o) - M_{\mathrm{zoo,det}} Z^2 \quad \text{(A2)}$$

GMDD
4, 289–342, 2011

Nutrients

$$\frac{\partial \mathrm{NO_3}}{\partial t} + w\frac{\partial \mathrm{NO_3}}{\partial z} - \frac{\partial}{\partial z}\left[k_\mathrm{v}\frac{\partial \mathrm{NO_3}}{\partial z}\right] - \frac{1}{\tau}\left(\mathrm{NO_3^*} - \mathrm{NO_3}\right) = -\pi_2 \sum_i \left(\mu_{i,\mathrm{phy}} P_i\right) + A_n\left(\frac{\mathrm{NH_4}}{0.07 + \mathrm{NH_4}}\right) \tag{A3}$$

$$\frac{\partial \mathrm{NH_4}}{\partial t} + w\frac{\partial \mathrm{NH_4}}{\partial t} - \frac{\partial}{\partial z}\left[k_\mathrm{v}\frac{\partial \mathrm{NH_4}}{\partial z}\right] = a_p M_{\mathrm{phy,det}} \sum_i (P_i - P_{i,o}) + R_{\mathrm{phy,NO_3}} \sum_i (P_i - P_{i,o}) - \pi_1 \sum_i \left(\mu_{i,\mathrm{phy}} P_i\right) + \mathrm{rem}\ \det_N + a_z M_{\mathrm{zoo,det}} Z^2 + E_{\mathrm{zoo,NO_3}}(Z - Z_o) - A_n\left(\frac{\mathrm{NH_4}}{0.07 + \mathrm{NH_4}}\right) + k_{rn}\mathrm{DON} \tag{A4}$$

$$\frac{\partial \mathrm{PO_4}}{\partial t} + w\frac{\partial \mathrm{PO_4}}{\partial t} - \frac{\partial}{\partial z}\left[k_\mathrm{v}\frac{\partial \mathrm{PO_4}}{\partial z}\right] = \frac{1}{\tau}\left(\mathrm{PO_4^*} - \mathrm{PO_4}\right) + k_{rp}\mathrm{DOP} + \mathrm{remdet}_P + \left[\left(a_p M_{\mathrm{phy,det}} + R_{\mathrm{phy,NO_3}}\right)\sum_i (P_i - P_{i,o}) - \sum_i \left(\mu_{i,\mathrm{phy}} P_i\right) + a_z M_{\mathrm{zoo,det}} Z^2 + E_{\mathrm{zoo,NO_3}}(Z - Z_o)\right]\frac{1}{r_1} \tag{A5}$$

$$\frac{\partial \mathrm{SiO_2}}{\partial t} + w\frac{\partial \mathrm{SiO_2}}{\partial t} - \frac{\partial}{\partial z}\left[k_\mathrm{v}\frac{\partial \mathrm{SiO_2}}{\partial z}\right] - \frac{1}{\tau}\left(\mathrm{SiO_2^*} - \mathrm{SiO_2}\right) = \left[\left(a_p M_{\mathrm{phy,det}} + R_{\mathrm{phy,NO_3}}\right)(P_1 - P_{1,o}) - \sum_i \left(\mu_{2,\mathrm{phy}} P_2\right) + a_z M_{\mathrm{zoo,det}} Z^2 + E_{\mathrm{zoo,NO_3}}(Z - Z_o)\right]\left(\frac{\mathrm{S}}{\mathrm{N}}\right)_{\mathrm{Red}} + k_{rp}\mathrm{DOS} + \mathrm{remdet}_S \tag{A6}$$

GMDD
4, 289–342, 2011

Dissolved organic matter

$$\frac{\partial \mathrm{DON}}{\partial t} + w\frac{\partial \mathrm{DON}}{\partial z} - \frac{\partial}{\partial z}\left[k_{\mathrm{v}}\frac{\partial \mathrm{DON}}{\partial z}\right] = a'_p M_{\mathrm{phy,det}} \sum_i (P_i - P_{i,o}) + a'_Z M_{\mathrm{zoo,det}} Z^2 - k_{rn}\mathrm{DON} \tag{A7}$$

$$\frac{\partial \mathrm{DOP}}{\partial t} + w\frac{\partial \mathrm{DOP}}{\partial z} - \frac{\partial}{\partial z}\left[k_{\mathrm{v}}\frac{\partial \mathrm{DOP}}{\partial z}\right] = \frac{1}{r_1}\left[a'_p M_{\mathrm{phy,det}} \sum_i (P_i - P_{i,o}) + a'_Z M_{\mathrm{zoo,det}} Z^2\right] - k_{rp}\mathrm{DOP} \tag{A8}$$

$$\frac{\partial \mathrm{DOC}}{\partial t} + w\frac{\partial \mathrm{DOC}}{\partial z} - \frac{\partial}{\partial z}\left[k_{\mathrm{v}}\frac{\partial \mathrm{DOC}}{\partial z}\right] = \frac{1}{\rho}\left[0.15 \sum_i (\mu_{i,\mathrm{phy}} P_i) + a'_p M_{\mathrm{phy,det}} \sum_i (P_i - P_{i,o}) + a'_Z M_{\mathrm{zoo,det}} Z^2\right]\left(\frac{\mathrm{C}}{\mathrm{N}}\right)_{\mathrm{Red}} - k_{rc}\mathrm{DOC} \tag{A9}$$

Detritus

$$\frac{\partial \det_N}{\partial t} + w\frac{\partial \det_N}{\partial z} - \frac{\partial}{\partial z}\left[k_{\mathrm{v}}\frac{\partial \det_N}{\partial z}\right] = (1 - a_p - a'_p)\left[M_{\mathrm{phy,det}} \sum_i (P_i - P_{i,o})\right] + (1-\gamma)\sum_i (\mu_{i,\mathrm{zoo}} Z) + (1 - a_z - a'_z) M_{\mathrm{zoo,det}} Z^2 - w_{\mathrm{det}}\frac{\partial \det_N}{\partial z} - \mathrm{rem}\ \det_N \tag{A10}$$

$$\frac{\partial \det_P}{\partial t} + w\frac{\partial \det_P}{\partial z} - \frac{\partial}{\partial z}\left[k_{\mathrm{v}}\frac{\partial \det_P}{\partial z}\right] = (1 - a_p - a'_p)\left[M_{\mathrm{phy,det}} \sum_i (P_i - P_{i,o})\frac{1}{r_1}\right] + \left[(1-\gamma)\sum_i (\mu_{i,\mathrm{zoo}} Z) + (1 - a_z - a'_z) M_{\mathrm{zoo,det}} Z^2\right]\frac{1}{r_1} - w_{\mathrm{det}}\frac{\partial \det_P}{\partial z} - \mathrm{rem}\ \det_P \tag{A11}$$

GMDD
4, 289–342, 2011

$$\frac{\partial \mathrm{det}_S}{\partial t} + w\frac{\partial \mathrm{det}_S}{\partial z} - \frac{\partial}{\partial z}\left[k_\mathrm{v}\frac{\partial \mathrm{det}_S}{\partial z}\right] = [(1-a_p-a'_p)M_{\mathrm{phy,det}}(P_1-P_{1,o}) + (1-\gamma)(\mu_{2,\mathrm{zoo}}Z) + (1-a_z-a'_z)M_{\mathrm{zoo,det}}Z^2]\left(\frac{\mathrm{S}}{\mathrm{N}}\right)_{\mathrm{Red}} - w_{\mathrm{det}}\frac{\partial \mathrm{det}_S}{\partial z} - \mathrm{rem\ det}_S \tag{A12}$$

$$\frac{\partial \mathrm{det}_{\mathrm{CaCO_3}}}{\partial t} + w\frac{\partial \mathrm{det}_{\mathrm{CaCO_3}}}{\partial z} - \frac{\partial}{\partial z}\left[k_\mathrm{v}\frac{\partial \mathrm{det}_{\mathrm{CaCO_3}}}{\partial z}\right] = \left(\frac{\mathrm{C}}{\mathrm{N}}\right)_{\mathrm{Coc}}[(1-a_p-a'_p)M_{\mathrm{phy,det}}(P_3-P_{3,o}) + (1-\gamma)(\mu_{3,\mathrm{zoo}}Z) + (1-a_z-a'_z)M_{\mathrm{zoo,det}}Z^2] - w_{\mathrm{det}}\frac{\partial \mathrm{det}_{\mathrm{CaCO_3}}}{\partial z} \tag{A13}$$

Calcite

$$\frac{\partial \mathrm{CaCO_3}}{\partial t} + w\frac{\partial \mathrm{CaCO_3}}{\partial z} - \frac{\partial}{\partial z}\left[k_\mathrm{v}\frac{\partial \mathrm{CaCO_3}}{\partial z}\right] = P_{\mathrm{CaCO_3}} - \lambda^*_{\mathrm{CaCO_3}}\mathrm{CaCO_3} - w_{\mathrm{det}}\frac{\partial \mathrm{CaCO_3}}{\partial z} \tag{A14}$$

Dissolved inorganic carbon

$$\frac{\partial \mathrm{DIC}}{\partial t} + w\frac{\partial \mathrm{DIC}}{\partial z} - \frac{\partial}{\partial z}\left[k_\mathrm{v}\frac{\partial \mathrm{DIC}}{\partial z}\right] - \frac{1}{\tau}(\mathrm{DIC}^* - \mathrm{DIC}) = \delta(z)\frac{\mathrm{FCO_2}}{\rho} - \frac{N_P}{\rho} + \frac{1}{S_o}\frac{\partial S}{\partial t}\mathrm{DIC} + \frac{1}{\rho}\left[\lambda^*_{\mathrm{CaCO_3}}\mathrm{CaCO_3} - P_{\mathrm{CaCO_3}}\right] \tag{A15}$$

Alkalinity

$$\frac{\partial \mathrm{TA}}{\partial t} + w\frac{\partial \mathrm{TA}}{\partial z} - \frac{\partial}{\partial z}\left[k_\mathrm{v}\frac{\partial \mathrm{TA}}{\partial z}\right] - \frac{1}{\tau}(\mathrm{TA}^* - \mathrm{TA}) = \frac{N_P}{\rho} + \frac{1}{S_o}\frac{\partial S}{\partial t}TA + \frac{2}{\rho}\left[\lambda^*_{\mathrm{CaCO_3}}\mathrm{CaCO_3} - P_{\mathrm{CaCO_3}}\right] \tag{A16}$$

GMDD
4, 289–342, 2011

Calcite production, calcification/organic carbon production ratio (R_{CaCO_3}) and calcite dissolution rate (λ_{CaCO_3})

$$P_{CaCO_3} = R^*_{CaCO_3}\left[\frac{C}{N}\right]_{Coc}\left[\mu_{3,phyto}P_3 - 0.5E_{zoo,NO_3}(Z - Z_o) \quad -M_{phy,det}(P_3 - P_{3,o})\right] \quad \text{(A17a)}$$

$$R^*_{CaCO_3} = R_{CaCO_3}F_{3,phy}(E)\min\left[N_{lim}, \frac{PO_4}{k_{P1} + PO_4}\right] \quad \times \max\left[0.0001, \frac{T}{2+T}\right]\max\left[1, \frac{P_3}{2}\right]$$

$$\lambda^*_{CaCO_3} = \lambda_{CaCO_3}\frac{\Delta CO_3}{k_{CaCO_3} + \Delta CO_3} \quad \text{(A17b)}$$

$$\Delta CO_3 = \max(0, CO^{2-}_{sat} - CO^{2-})$$

Net community production

$$N_p = \left(\frac{C}{N}\right)_{Red}[\mu_{1,phy}P_1 + \mu_{2,phy}P_2 - (a_pM_{phy,det} + R_{phy,NO_3})\{(P_1 - P_{1;o}) + (P_2 - P_{2;o})\} - a_zM_{zoo,det}Z^2 - R_{zoo,NO_3}(Z - Z_o) - \text{rem det}_N] - k_{rc}DOC + \left(\frac{C}{N}\right)_{Coc}\mu_{3,phy}P_3 \quad \text{(A18)}$$

Oxygen

$$\frac{\partial O_2}{\partial t} + w\frac{\partial O_2}{\partial z} - \frac{\partial}{\partial z}\left[k_v\frac{\partial O_2}{\partial z}\right] = \delta(z)\frac{FO_2}{\rho} + \frac{N_P}{\rho}\left(\frac{O_2}{N}\right)_{Red} \quad \text{(A19)}$$

Nutrient limitation

$$N_{lim} = NH4_{lim} + NO3_{lim} \quad \text{(A20)}$$

GMDD
4, 289–342, 2011

$$NO_{3_{lim}} = \frac{NO_3}{(K_{NO_3} + NO_3)} \frac{(1 - NH_4)}{(K_{NH_4} + NH_4)} \tag{A21}$$

$$NH_{4_{lim}} = \frac{NH_4}{(K_{NH_4} + NH_4)} \tag{A22}$$

$$\pi_1 = \frac{NH_{4_{lim}}}{NH_{4_{lim}} + NO_{3_{lim}}} \tag{A23}$$

$$\pi_2 = \frac{NO_{3_{lim}}}{NH_{4_{lim}} + NO_{3_{lim}}} \tag{A24}$$

Irradiance model

The total (infrared plus visible) solar radiation is obtained using the Frouin model (Frouin et al., 1989). This model provides the total radiation and the photosynthetically available radiation (PAR). The infrared (I_{IR}) component is obtained by subtracting the PAR component from the total solar radiation. Using a spectral model for PAR (Gregg and Carder, 1990), the spectral PAR component $I_{PAR}(\lambda)$ can be determined. The infrared component (for mixed layer model only) and the PAR component (mixed layer and biogeochemical model) of the penetrating irradiance are obtained from

$$I_{IR}(z) = I_{IR}(z - \Delta z)\exp[-a_{IR}\Delta z] \tag{A25}$$

$$I_{PAR}(\lambda, z) = I(\lambda, z - \Delta z)\exp[-(a_w(\lambda) + a_{ph}(\lambda))\Delta z] \tag{A26}$$

where a_{IR} (3.75 m^{-1}) is the attenuation coefficient for infrared radiation, and $a_w(\lambda)$ and $a_{ph}(\lambda)$ are the wavelength-dependent light attenuation coefficients for water and phytoplankton, respectively. The water and chlorophyll-dependent attenuation coefficients from Morel (1988) were used in the model for this study. The dissolved matter attenuation coefficients, $a_{dm}(\lambda)$, are calculated by applying the IOP (inherent optical properties)

GMDD
4, 289–342, 2011

model of Garver and Siegel (1997), which uses water leaving radiances from 6 SeaWiFS bands as input (level 3 binned monthly composites). The IOP model calculates the attenuation coefficient due to dissolved matter for the 443nm wavelength. The attenuation coefficients for other wavelengths are obtained from

$$a_{\mathrm{dm}}(\lambda) = a_{\mathrm{dm}}(443)\exp[S(\lambda - 443)] \tag{A27}$$

where the exponential decay constant, S, is chosen to be 0.02061. A correction is applied to the downward irradiance pathway to account for seawater light refraction following Snell's law. After some algebraic manipulations, the correction is applied to Δz as follows

$$\Delta z' = \frac{\Delta z}{\cos\beta} \tag{A28}$$

$$\beta = a\sin\left[\frac{\alpha_{\mathrm{z}}}{n_{\mathrm{s}}}\right] \tag{A29}$$

where α_{z} is the solar zenith angle, and n_{s} is the seawater refraction coefficient which is expressed as a function of salinity and temperature adapted from Table 3.12 of Neumann and Pierson (1966) as

$$n_s = 10^{-6}(285.77 - 15.65T + 197.67S) + 1.333338 \tag{A30}$$

Ammonium nitrification

$$\begin{aligned} A_n &= A_n^{\max}\left(1 - \frac{D - D_{\min}}{D - D_{\min} - K_D}\right) \\ D &= \int_{t=0}^{t=24}\int_{\lambda=300}^{\lambda=470} I(\lambda,t)\alpha_S(\lambda)\,d\lambda\,dt \end{aligned} \tag{A31}$$

GMDD
4, 289–342, 2011

Phytoplankton growth

$$\mu_{i,\mathrm{phy}}(\mathrm{NO_3},\mathrm{PO_4},\mathrm{SiO_2},E) = F_{i,\mathrm{phy}}(E) \times \min\left[\mathrm{N_{lim}}, \frac{\mathrm{PO_4}}{\mathrm{k_{PO_4}} + \mathrm{PO_4}}, \frac{\mathrm{SiO_2}}{\mathrm{k_{SiO_2}} + \mathrm{SiO_2}}\right] \tag{A32}$$

$$F_{i,\mathrm{phy}}(I) = \frac{\mu^{\max}_{i,\mathrm{phy}} \alpha_i I}{\sqrt{\left(\mu^{\max}_{i,\mathrm{phy}}\right)^2 + (\alpha_i I)^2}} \tag{A33}$$

$r_1 = 14$ is N:P

Zooplankton grazing

$$\mu_{\mathrm{zoo}}(P_i) = \mu^{\max}_{\mathrm{zoo}} \frac{P_i^2}{k_{\mathrm{phy}} + P_i^2} \tag{A34}$$

Primary production

$$\mathrm{PP} = \left[\left(\mu_{1,\mathrm{phy}} P_1 + \mu_{2,\mathrm{phy}} P_2\right)\left(\frac{\mathrm{C}}{\mathrm{N}}\right)_{\mathrm{Red}} + \mu_{3,\mathrm{phy}} P_3 \left(\frac{\mathrm{C}}{\mathrm{N}}\right)_{\mathrm{Coc}}\right] \mathrm{C_{MW}}$$
$$\left(\frac{\mathrm{C}}{\mathrm{N}}\right)_{\mathrm{Red}} = 6.625 \quad \left(\frac{\mathrm{C}}{\mathrm{N}}\right)_{\mathrm{Coc}} = 9.4 \quad \mathrm{C_{MW}} = 12 \tag{A35}$$
$$\left(\frac{\mathrm{Si}}{\mathrm{N}}\right)_{\mathrm{Red}} = \frac{15}{16}$$

The C:N ratio for coccolithophores (Coc) of 9.4 is the average from the reported range of 5.81 to 13.05 in Fernandez et al. (1993).

GMDD
4, 289–342, 2011

Chlorophyll and Chl:N ratio

The model chlorophyll is calculated following the photoadaptation scheme for Chl:N ratio of (Doney et al., 1996):

$$\mathrm{Chl}-a = \mathrm{Chl:N}\sum_i P_i \tag{A36}$$

$$\begin{aligned} \mathrm{Chl:N} &= \mathrm{Chl:N}^{\max} - (\mathrm{Chl:N}^{\max} - \mathrm{Chl:N}^{\min})\frac{I_{\mathrm{PAR}}}{I^*} \quad I_{\mathrm{PAR}} < I^* \\ \mathrm{Chl:N} &= \mathrm{Chl:N}^{\min} \quad I_{\mathrm{PAR}} \geq I^* \end{aligned} \tag{A37}$$

The subscripts phy, zoo, and det refer to phytoplankton, zooplankton, and detritus, respectively. Table A1 defines the model state variables and Table A2 provides the definition of the model parameters and values used.

Model forcing and relaxation approach

The terms $\delta(z)\mathrm{FCO_2}/\rho$ and $\delta(z)\mathrm{FO_2}/\rho$, in Eqs. (A15) and (A19), respectively, represent the CO_2 and O_2 sea-air fluxes at the surface. The Kroenecker delta ($\delta[z=0]=1$; $\delta[z>0]=0$) is used to denote that carbon dioxide and oxygen fluxes (FCO_2 and FO_2, respectively) are only applied at the sea-air interface. The following formulations for the CO_2 and O_2 gas transfer were applied in the form of flux boundary conditions (FCO_2 and FO_2 in mmol m^{-2} yr^{-1}) at the sea-air interface:

$$\begin{aligned} \mathrm{FCO_2} &= K_o \alpha \Delta p\mathrm{CO_2} \\ \mathrm{FO_2} &= K_o\left[\mathrm{O_2^*} - \mathrm{O_2}\right] \end{aligned} \tag{A38}$$

where, K_o is the gas transfer velocity, in m d^{-1}, which is a function of water temperature and wind speed (Wanninkhof, 1992), α is the CO_2 solubility in seawater (in mmol m^{-3} µatm), which is a function of temperature and salinity (Weiss, 1974), $\Delta p\mathrm{CO_2}$

GMDD
4, 289–342, 2011

(in µatm) is the difference between sea and air pCO_2, and O_2^* is the oxygen saturation concentration (in mmol m^{-3}) in seawater, which is a function of temperature and atmospheric pressure (Weiss, 1970).

We adopt the following relationship between gas transfer and wind speed (W) (Wanninkhof, 1992) using the NCEP 6 hourly winds:

$$K_o = 0.31W^2(Sc/660)^{-1/2} \tag{A39}$$

where Sc is the Schmidt number of CO_2 or O_2 (Wanninkhof, 1992).

To account for horizontal advective processes of heat and salt within deeper layers of the 1-D mixed layer model, temperature and salinity are assimilated from the 3-D model using a straightforward approach. The approach consists of relaxing the temperature and salinity profiles calculated by the 1-D mixed layer model to the pre-calculated values provided by the 3-D model below 500 m when the MLD exceeds that depth. The assimilation of T and S is done using a Newtonian relaxation (nudging) method (Bauer and Wulfmeyer, 2009) with a relaxation time scale (τ) of 10 days for T and 30 days for S.

A similar relaxation approach is used for nitrate, phosphate, and silicate, except that the nutrient values originate from T-dependent equations obtained from T, NO_3, PO_4, and SiO_2 climatologic monthly profiles (0–500 m) from the World Ocean Atlas 2005 at the model site. The total number of data points is 168 (N = 14depths × 12 months). The equations are:

$$\begin{aligned} NO_3^* &= -2.253(\pm 0.169)T + 29.92(\pm 1.21) \quad r^2 = 0.814 \quad \text{RMSE} = 1.258 \\ PO_4^* &= -0.1333(\pm 0.0095)T + 1.884(\pm 0.068) \quad r^2 = 0.836 \quad \text{RMSE} = 0.0707 \\ SiO_2^* &= -1.479(\pm 0.135)T + 17.37(\pm 0.98) \quad r^2 = 0.735 \quad \text{RMSE} = 1.012 \end{aligned} \tag{A40}$$

The relaxation is done for depth below the mixed layer with $\tau = 0.$ days. As previously mentioned in the main text, DIC and TA in the model deeper layers are nudged to the values obtained from regression equations using CARINA in situ data within the depth range of 200 to 1000 m. The equations are:

GMDD
4, 289–342, 2011

$$\mathrm{DIC}^* = nC_T \times S/35$$
$$nC_T = 1962.6 - 14.6204(T-20) - 0.1371(T-20)^2 \quad \text{(A41)}$$
$$r^2 = 0.762, \mathrm{RMSE} = 10.15, N = 148$$

$$\mathrm{TA}^* = 2311.6 + 46.4153(S-35) + 56.4425(S-35)^2 - 0.0456(T-20) - 0.0387(T-20)^2 \quad \text{(A42)}$$
$$r^2 = 0.448, \mathrm{RMSE} = 4.15, N = 123$$

Appendix B

Compensation of variable ratio of Zeu to MLD on PP

For integration of daily primary production (PP; mg carbon $\mathrm{m}^{-2}\,\mathrm{d}^{-1}$) we used MRI's (the Marine Research Institute in Reykjavík, Iceland) measurements on chlorophyll *a* (Chl-*a*; $\mathrm{mg\,m}^{-3}$) from water samples, results of PvsE-experiments ($P^B_{\max}$ and α), surface irradiation derived from satellite records and the CTD profiles, for deciding the depth of the surface mixed layer (MLD).

The daily primary production (PP; mg carbon $\mathrm{m}^{-2}\,\mathrm{d}^{-1}$) is integrated both with respect to time of the day (t), i.e. for each half hour from midnight to local noon, times two, and with respect to the depth of the water column, i.e. for each meter (z) from the surface to the bottom of the euphotic zone, using the saturation equation (Jassby and Platt, 1976):

$$\mathrm{PP} = \iint \left[B(z) P^B_{\max} \tanh(\alpha_B \mathrm{PAR}(z,t)/P^B_{\max}) \right] dz\,dt \quad \text{(B1)}$$

where $B(z)$ is the relevant biomass profile (mg Chl-*a* m^{-3}), and the Chl-*a* specific initial slope of the photosynthetic rate α_B (mg C [mg Chl-*a*]$^{-1}$ h^{-1} W^{-1} m^2) and maximum production rate at optimal light intensity $\mathrm{P}^B_{\max}$ (mg C [mg Chl-*a*]$^{-1}$ h^{-1}) are derived from the corresponding P-I experiments. The depth distribution of Chl-*a* ($B(0 \le z \le \mathrm{Zeu})$) is

GMDD
4, 289–342, 2011

assumed to be static during the day. The daily photosynthetically active radiation at the surface (PAR_0; μmol photons $m^{-2}\,s^{-1}$) changes according to a sine function over the daylight hours, while the attenuation of light with depth, PAR (z,t), varies with respect to depth (z; meters) according to:

$$PAR(z,t) = PAR(0,t)\exp(-kz), \tag{B2}$$

where the attenuation coefficient (k) is a function of Chl-a. Generally, k is averaged for the water column, and may be calculated according to the empirical relation of light attenuation and Secchi depth (SD), $k = 1.7/SD$ (Poole and Atkins, 1929). Combining that with an empirical relation between Chl-a in the uppermost 10 m and Secchi depth, $SD = 10.4 \times (Chl-a)^{-0.25}$ (Gudmundsson, 2002), gives $k = 0.163/(Chl\text{-}a)^{-0.25}$. Accordingly, one may rewrite Eq. (B2) as:

$$PAR(z) = PAR(z-1)\exp\left[-0.163/((Chl-a(z-1) + Chl-a(z))/2)^{-0.25}\right] \tag{B3}$$

for calculations of PAR, as a function of the depth distribution of Chl-a.

Comparison of the depth level for 1% of the surface light ($Z_{1\%}$), calculated according to the averaged k, using Eq. (B2), with that calculated stepwise for each meter depth according to Eq. (B3) and the distribution of chlorophyll-a concentrations, reveals quite similar results. The latter approach is preferred as it allows variations in attenuation with depth in accordance with measured Chl-a, and thus in calculated productivity.

The lower limit for credible measured Chl-a from water samples is 0.05 mg m^{-3} and at that level k approaches the attenuation coefficient for clear water according to Eq. (B3). Therefore, 0.05 was applied as minimum Chl-a in our calculations.

The spectral change in surface irradiation during a day was not accounted for and thus the effect of that on light attenuation with depth was ignored. Accordingly, Eq. (B3) only needs to be solved with respect to depth.

In accordance with the definition of the euphotic zone (Zeu), it is assumed that all photosynthetic assimilation of carbon by photosynthesis takes place above the $Z_{1\%}$ (on daily basis), i.e. from the surface and down to the bottom of the euphotic zone

GMDD
4, 289–342, 2011

(Zeu$\equiv Z_{1\%}$). Furthermore, it is assumed that any phytoplankton cell inside the mixing layer may move arbitrarily between the boundaries of a defined mixed layer during a day, regardless of the assumption that the depth distribution of chlorophyll concentrations is considered static. Clearly, there is no need for correction of the integrated PP if Zeu equals the MLD. However, that is rarely the case and this analytical model obviously does not account for vertical mixing outside the Zeu. For example, if the daily production integrated for the euphotic zone is mixed in a layer that is twice as deep, where the light intensities in half the depth of the mixed layer is below the compensation light level for carbon assimilation, then the daily production was probably overestimated by a factor of two.

Typically, most of the carbon assimilation of phytoplankton photosynthesis in the North Atlantic Oceans takes place in a surface layer, above the MLD, kept turbulent by the prevailing wind forces in the area. Below the surface mixed layer one may have one or more layers, but as the light availability at greater depth severely limits the primary productivity, only two layers will be considered here. First, we define the conditions: (a) Zeu $\leq$ MLD and (b) Zeu $>$ MLD.

One way to compensate the effects of vertical mixing with respect to the changes in both Zeu and MLD, while integrating the daily primary production, is to moderate the available PAR at the surface. That is reasonable as the mixing affects the average of available light intensity for particles moving around in the water column. A plausible compensation for the changes in scenario A may be acquired by multiplying the PAR_0 with the ratio Zeu/MLD. In line with that, one may look at scenario B as the sum of two separate layers, where the upper layer does not need compensation and the lower layer is treated as in scenario A, when the upper layer has been dealt with and cut off. As the bottom depth of the lower layer is frequently not known, a fixed depth of 150 m is used for the purpose.

GMDD
4, 289–342, 2011

Thus, in an attempt to compensate for effects of vertical mixing in the water column on PP the PAR(z,t) in Eq. (B1) was modified with respect to Zeu and MLD accordingly:

$$\mathrm{PAR}(z,t) = \left\{ \begin{array}{l} \text{for Zeu} \leq \text{MLD}, \\ \dfrac{\text{Zeu}}{\text{MLD}} \mathrm{PAR}(0,t) e^{(-kz)}, 0 < z \leq \text{Zeu} \\ \text{for Zeu} > \text{MLD}, \\ \mathrm{PAR}(0,t) e^{(-kz)}, 0 < z \leq \text{MLD} \\ \dfrac{(\text{Zeu} - \text{MLD})}{(150 - \text{MLD})} \mathrm{PAR}(0,t) e^{(-kz)}, z > \text{MLD} \end{array} \right\} \tag{B4}$$

Acknowledgements. This project was supported by the NASA Ocean Biology and Biogeochemistry Program. We want to acknowledge the MarEco (2003) project sponsored by Census of Marine Life and the NAB 2008 project (US NSF grants OCE 0628107 and 0628379), for supplying primary production data and the project A-CARB of the Research Council of Norway. We also want to acknowledge the SURATLANTE project, which is supported by the Institut National de Sciences de l'Univers (INSU) in France, and the MarProd program sponsored by the Natural Environment Research Council (UK). Continuous Plankton Recorder data were obtained from the Sir Alistair Hardy Foundation for Ocean Sciences. We would like to acknowledge the support of the Reykjavik Marine Research Institute (MRI) personnel (Sólveig Ólafsdóttir and Magnus Danielsen).

References

Armstrong, R. A., Lee, C., Hedges, J. I., Honjo, S., and Wakeham, S. G.: A new, mechanistic model for organic carbon fluxes in the ocean based on the quantitative association of POC with ballast minerals, Deep-Sea Res. Pt. II, 49, 219–236, 2002.

Aumont, O. and Bopp, L.: Globalizing results from ocean in situ iron fertilization studies, Global Biogeochem. Cy., 20, GB2017, doi:10.1029/2005GB002591, 2006.

Bailey, D. A., Rhines, P. B., and Hakkinen, S.: Formation and pathways of North Atlantic deep water in a coupled ice-ocean model of the Arctic-North Atlantic Oceans, Clim. Dynam., 25, 497–516, 2005.

Balch, W. M., Holligan, P. M., and Kilpatrick, K. A.: Calcification, photosynthesis and growth of the bloom-forming coccolithophore, *Emiliania huxleyi*, Cont. Shelf Res., 12, 1353–1374, 1992.

Balch, W., Drapeau, D., Bowler, B., and Booth, E.: Prediction of pelagic calcification rates using satellite measurements, Deep-Sea Res. Pt. II, 54, 478–495, 2007.

Bauer, H. S. and Wulfmeyer, V.: Validation of components of the water cycle in the ECHAM4 general circulation model based on the Newtonian relaxation technique: a case study of an intense winter cyclone, Meteorol. Atmos. Phys., 104, 135–162, 2009.

Behrenfeld, M. J., Boss, E., Siegel, D. A., and Shea, D. M.: Carbon-based ocean productivity and phytoplankton physiology from space, Global Biogeochem. Cy., 19, GB1006, doi:10.1029/2004GB002299, 2005.

Chierici, M., Olsen, A., Johannessen, T., Trinanes, J., and Wanninkhof, R.: Algorithms to estimate the carbon dioxide uptake in the Northern North Atlantic using shipboard observations, satellite and ocean analysis data, Deep-Sea Res. Pt. II, 56, 630–639, 2009.

Chung, S. N., Lee, K., Feely, R. A., Sabine, C. L., Millero, F. J., Wanninkhof, R., Bullister, J. L., Key, R. M., and Peng, T. H.: Calcium carbonate budget in the Atlantic Ocean based on water column inorganic carbon chemistry, Global Biogeochem. Cy., 17(4), 1093, doi:10.1029/2002GB002001, 2003.

Corbiere, A., Metzl, N., Reverdin, G., Brunet, C., and Takahashi, A.: Interannual and decadal variability of the oceanic carbon sink in the North Atlantic subpolar gyre, Tellus B, 59, 168–178, 2007.

Doney, S. C., Glover, D. M., and Najjar, R. G.: A new coupled, one-dimensional biological-physical model for the upper ocean: applications to the JGOFS Bermuda Atlantic time-series study (BATS) site, Deep-Sea Res. Pt. II, 43, 591–624, 1996.

Feely, R. A., Sabine, C. L., Lee, K., Berelson, W., Kleypas, J., Fabry, V. J., and Millero, F. J.: Impact of anthropogenic CO_2 on the $CaCO_3$ system in the oceans, Science, 305, 362–366, 2004.

Fernandez, E., Boyd, P., Holligan, P. M., and Harbour, D. S.: Production of organic and inorganic carbon within a large-scale coccolithophore bloom in the Northeast Atlantic Ocean, Mar. Ecol.-Prog. Ser., 97, 271–285, 1993.

Francois, R., Honjo, S., Krishfield, R., and Manganini, S.: Factors controlling the flux of organic carbon to the bathypelagic zone of the ocean, Global Biogeochem. Cy., 16(4), 1087, doi:10.1029/2001GB001722, 2002.
Frouin, R., Lingner, D. W., Gautier, C., Baker, K. S., and Smith, R. C.: A simple analytical formula to compute clear sky total and photosynthetically available solar irradiance at the ocean surface, J. Geophys. Res.-Oceans, 94, 9731–9742, 1989.
Gallegos, C. L. and Platt, T.: Vertical advection of phytoplankton and productivity estimates: a dimensional analysis, Mar. Ecol.-Prog. Ser., 26, 125–134, 1985.
Garver, S. A., and Siegel, D. A.: Inherent optical property inversion of ocean color spectra and its biogeochemical interpretation. 1. Time series from the Sargasso Sea, J. Geophys. Res.-Oceans, 102, 18607–18625, 1997.
Gehlen, M., Gangstø, R., Schneider, B., Bopp, L., Aumont, O., and Ethe, C.: The fate of pelagic $CaCO_3$ production in a high CO_2 ocean: a model study, Biogeosciences, 4, 505–519, doi:10.5194/bg-4-505-2007, 2007.
Gregg, W. W. and Carder, K. L.: A simple spectral solar irradiance model for cloudless maritime atmospheres, Limnol. Oceanogr., 35, 1657–1675, 1990.
Gudmundsson, K.: Long-term variation in phytoplankton productivity during spring in Icelandic waters, ICES J. Mar. Sci., 55, 635–643, 1998.
Gudmundsson, K., Gislason A., Olafsson J., Thorisson K., Bjornsdottir R., Steingrimsson, S. A., Olafsdottir, S. R., and Kaasa O.: Ecology of Eyjafjordur Project, Marine Research Institute, Report No. 106, Reykjavik, 2002.
Hakkinen, S.: Simulated interannual variability of the Greenland Sea deep-water formation and its connection to surface forcing, J. Geophys. Res.-Oceans, 100, 4761–4770, 1995.
Hakkinen, S. and Proshutinsky, A.: Freshwater content variability in the Arctic Ocean, J. Geophys. Res.-Oceans, 109, CO3051, doi:10.1029/2003JC001940, 2004.
Henson, S. A., Sanders, R., Holeton, C., and Allen, J. T.: Timing of nutrient depletion, diatom dominance and a lower-boundary estimate of export production for Irminger Basin, North Atlantic, Mar. Ecol.-Prog. Ser., 313, 73–84, 2006.
Henson, S. A., Dunne, J. P., and Sarmiento, J. L.: Decadal variability in North Atlantic phytoplankton blooms, J. Geophys. Res.-Oceans, 114, CO4013, doi:10.1029/2009JC005139, 2009.
Holliday, N. P., Waniek, J. J., Davidson, R., Wilson, D., Brown, L., Sanders, R., Pollard, R. T., and Allen, J. T.: Large-scale physical controls on phytoplankton growth in the Irminger Sea

GMDD
4, 289–342, 2011

– Part I: Hydrographic zones, mixing and stratification, J. Marine Syst., 59, 201–218, 2006.
Holligan, P. M., Fernandez, E., Aiken, J., Balch, W. M., Boyd, P., Burkill, P. H., Finch, M., Groom, S. B., Malin, G., Muller, K., Purdie, D. A., Robinson, C., Trees, C. C., Turner, S. M., and Vanderwal, P.: A biogeochemical study of the coccolithophore, *Emiliania huxleyi*, in the North Atlantic, Global Biogeochem. Cy., 7, 879–900, 1993a.
Holligan, P. M., Groom, S. B., and Harbour, D. S.: What controls the distribution of the coccolithophore, *Emiliania huxleyi*, in the North Sea?, Fish. Oceanogr., 2, 175–183, 1993b.
Jakobsson, J.: The North Icelandic herring fishery and environmental conditions 1960–1968, in: ICES Symposium, The Biological Basis of Pelagic Fish Stock Management, Aberdeen, Scotland, 102 pp., 1978.
Jassby, A. D. and Platt, T.: Mathematical formulation of relationship between photosynthesis and light for phytoplankton, Limnol. Oceanogr., 21, 540–547, 1976.
Jolliff, J. K., Kindle, J. C., Shulman, I., Penta, B., Friedrichs, M. A. M., Helber, R., and Arnone, R. A.: Summary diagrams for coupled hydrodynamic-ecosystem model skill assessment, J. Marine Syst., 76, 64–82, 2009.
Key, R. M., Tanhua, T., Olsen, A., Hoppema, M., Jutterström, S., Schirnick, C., van Heuven, S., Kozyr, A., Lin, X., Velo, A., Wallace, D. W. R., and Mintrop, L.: The CARINA data synthesis project: introduction and overview, Earth Syst. Sci. Data, 2, 105–121, doi:10.5194/essd-2-105-2010, 2010.
Klaas, C. and Archer, D. E.: Association of sinking organic matter with various types of mineral ballast in the deep sea: implications for the rain ratio, Global Biogeochem. Cy., 16(4), 1116, doi:10.1029/2001GB001765, 2002.
Koeve, W.: Upper ocean carbon fluxes in the Atlantic Ocean: the importance of the POC:PIC ratio, Global Biogeochem. Cy., 16(4), 1056, doi:10.1029/2001GB001836, 2002.
Maritorena, S., Siegel, D. A., and Peterson, A. R.: Optimization of a semianalytical ocean color model for global-scale applications, Appl. Optics, 41, 2705–2714, 2002.
Mellor, G. L. and Yamada, T.: Development of a turbulence closure model for geophysical fluid problems, Rev. Geophys. Space Ge., 20, 851–875, 1982.
Metzl, N., Corbiere, A., Reverdin, G., Lenton, A., Takahashi, T., Olsen, A., Johannessen, T., Pierrot, D., Wanninkhof, R., Olafsdottir, S. R., Olafsson, J., and Ramonet, M.: Recent acceleration of the sea surface fCO_2 growth rate in the North Atlantic subpolar gyre (1993–2008) revealed by winter observations, Global Biogeochem. Cy., 24, GB4004, doi:10.1029/2009GB003658, 2010.

GMDD
4, 289–342, 2011

Morel, A.: Optical modeling of the upper ocean in relation to its biogenous matter content (case-i waters), J. Geophys. Res.-Oceans, 93, 10749–10768, 1988.
Nelson, N. B., Siegel, D. A., Carlson, C. A., Swan, C., Smethie, W. M., and Khatiwala, S.: Hydrography of chromophoric dissolved organic matter in the North Atlantic, Deep-Sea Res. Pt. I, 54, 710–731, 2007.
Neumann, G. and Pierson, W. J.: Principles of Physical Oceanography, Prentice-Hall, Inc., Englewood Cliffs, NJ, 545 pp., 1966.
Nielsdóttir, M. C., Moore, C. M., Sanders, R., Hinz, D. J., and Achterberg, E. P.: Iron limitation of the postbloom phytoplankton communities in the Iceland Basin, Global Biogeochem. Cy., 23, GB3001, doi:10.1029/2008GB003410, 2009.
Olsen, A., Brown, K. R., Chierici, M., Johannessen, T., and Neill, C.: Sea-surface CO_2 fugacity in the subpolar North Atlantic, Biogeosciences, 5, 535–547, doi:10.5194/bg-5-535-2008, 2008.
Poole, H. H. and Atkins, W. R. G.: Photoelectric measurements of submarine illumination throughout the year, J. Mar. Biol. Assoc. UK, 16, 297–324, 1929.
Poulain, P. M., Warn-Varnas, A., and Niiler, P. P.: Near-surface circulation of the Nordic seas as measured by Lagrangian drifters, J. Geophys. Res.-Oceans, 101, 18237–18258, 1996.
Raitsos, D. E., Lavender, S. J., Pradhan, Y., Tyrrell, T., Reid, P. C., and Edwards, M.: Coccolithophore bloom size variation in response to the regional environment of the subarctic North Atlantic, Limnol. Oceanogr., 51, 2122–2130, 2006.
Reynolds, R. W. and Smith, T. M.: A high-resolution global sea-surface temperature climatology, J. Climate, 8, 1571–1583, 1995.
Signorini, S. R. and McClain, C. R.: Further Studies on Oceanic Biogeochemistry and Carbon Cycling, Technical Memorandum NASA/TM-2003-212245, NASA/TM-2003-212245, NASA Goddard Space Flight Center, Greenbelt, 212251 pp., 2003.
Signorini, S. R., McClain, C. R., and Christian, J. R.: Modeling biogeochemical-physical interactions and carbon flux in the Sargasso Sea (Bermuda Atlantic Time-series Study site), NASA Goddard Space Flight Center, Greenbelt, MD, 37, 2001a.
Signorini, S. R., McClain, C. R., Christian, J. R., and Wong, C. S.: Seasonal and interannual variability of phytoplankton, nutrients, TCO_2, pCO_2, and O_2 in the Eastern Subarctic Pacific, J. Geophys. Res., 106(C12), 31197–31215, 2001b.
Signorini, S. R., Hakkinen, S., Olsen, A., Gudmundsson, K., Omar, A. M., Olafsson, J., Reverdin, G., Henson, S. A., and McClain, C. R.: Decadal changes in the carbon sink and

GMDD
4, 289–342, 2011

ocean acidification in the Subpolar North Atlantic, in preparation, 2011.
Takahashi, T., Sutherland, S. C., Sweeney, C., Poisson, A., Metzl, N., Tilbrook, B., Bates, N., Wanninkhof, R., Feely, R. A., Sabine, C., Olafsson, J., and Nojiri, Y.: Global sea-air CO_2 flux based on climatological surface ocean *p*CO(2), and seasonal biological and temperature effects, Deep-Sea Res. Pt. II, 49, 1601–1622, 2002.
Waniek, J. J. and Holliday, N. P.: Large-scale physical controls on phytoplankton growth in the Irminger Sea, Part II: model study of the physical and meteorological preconditioning, J. Marine Syst., 59, 219–237, 2006.
Wanninkhof, R.: Relationship between wind-speed and gas-exchange over the ocean, J. Geophys. Res.-Oceans, 97, 7373–7382, 1992.
Weeks, A., Conte, M. H., Harris, R. P., Bedo, A., Bellan, I., Burkill, P. H., Edwards, E. S., Harbour, D. S., Kennedy, H., Llewellyn, C., Mantoura, R. F. C., Morales, C. E., Pomroy, A. J., and Turley, C. M.: The physical and chemical environment and changes in community structure associated with bloom evolution – the joint global flux study North Atlantic bloom experiment, Deep-Sea Res. Pt. II, 40, 347–368, 1993.
Weiss, R. F.: The solubility of nitrogen, oxygen, and argon in water and seawater, Deep-Sea Res., 17, 721–735, 1970.
Weiss, R. F.: Carbon dioxide in water and seawater: the solubility of a non-ideal gas, Mar. Chem., 2, 203–215, 1974.

GMDD
4, 289–342, 2011

Table 1. Summary of surface-ocean observed and model mean values and standard deviations (STD) for a selected number of variables. Only daily model values matching the nearest observed dates were chosen.

Variable	Observed		Model		N
	Mean	STD	Mean	STD	
SST (°C)	9.02	1.77	8.92	1.71	372
TA (μmol kg^{-1})	2309.26	8.88	2307.48	2.65	185
DIC (μmol kg^{-1})	2111.01	24.42	2106.75	27.63	243
NO_3 (μM)	9.38	3.27	7.00	4.68	102
SiO_2 (μM)	3.36	2.14	3.82	2.26	103
PO_4 (μM)	0.66	0.21	0.62	0.22	122
pCO_2 (μatm)	347.65	26.21	350.91	30.93	199
In situ PP (mg C m^{-2} d^{-1})	1016.48	740.42	319.60	225.10	55
Sat PP (mg C m^{-2} d^{-1})	207.85	323.19	220.63	235.28	114

GMDD
4, 289–342, 2011

Table A1. Ecosystem/Carbon model state variables definition, forcing strategy, and initial values.

Symbol	Units	Parameter	Forcing/Initial value
NO_3	mmol N m^{-3}	Dissolved inorganic nitrate	**Deep water NR
PO_4	mmol P m^{-3}	Dissolved inorganic phosphorus	**Deep water NR
SiO_2	mmol Si m^{-3}	Dissolved inorganic silica	**Deep water NR
NH_4	mmol N m^{-3}	Ammonium	0.05
O_2	µmol kg^{-1}	Dissolved oxygen	268.0
$CaCO_3$	mmol C m^{-3}	Calcium carbonate (calcite)	0.01
DIC	µmol kg^{-1}	Dissolved inorganic carbon	**Deep water NR + trend
TA	µmol kg^{-1}	Alkalinity	**Deep water NR
P_i	mmol N m^{-3}	Phytoplankton ($i = 1,2,3$)*	0.1
Z	mmol N m^{-3}	Zooplankton	0.1
DON	mmol N m^{-3}	Dissolved organic nitrogen	1.0/0.0
DOP	mmol P m^{-3}	Dissolved organic phosphorus	0.06/0.0
DOC	µmol C kg^{-1}	Labile dissolved organic carbon	15.0/0.0
det_N	mmol N m^{-3}	Detrital particulate nitrogen	0.001
det_P	mmol P m^{-3}	Detrital particulate phosphate	0.001
det_S	mmol Si m^{-3}	Detrital particulate silicate	0.001
det_{CaCO_3}	mmol $CaCO_3$ m^{-3}	Detrital particulate calcite	0.001

* Diatoms ($i = 1$), dinoflagellates ($i = 2$), and coccolithophores ($i = 3$).
** Deep layer Newtonian relaxation to values in Eqs. (A40)–(A42).

GMDD
4, 289–342, 2011

Table A2. Summary of model parameters used in the 1981–2008 simulation for the subpolar North Atlantic.

Parameter	Symbol	Units	Value
Diatoms (P_1)			
Maximum growth rate	$\mu_{phy,max}$	day^{-1}	1.2
Initial P-I slope	α_1	$(W\,m^{-2})^{-1}\,day^{-1}$	0.09
Nitrate half saturation constant	k_{NO_3}	$mmol\,N\,m^{-3}$	2.0
Phosphate half saturation constant	k_{PO_4}	$mmol\,P\,m^{-3}$	0.0015
Silicate half saturation constant	k_{SiO_2}	$mmol\,Si\,m^{-3}$	0.3
Respiration rate	R_{phy,NO_3}	day^{-1}	0.05
Mortality rate	$M_{phy,det}$	day^{-1}	0.05
Dinoflagellates (P_2)			
Maximum growth rate	$\mu_{phy,max}$	day^{-1}	0.65
Initial P-I slope	α_1	$(W\,m^{-2})^{-1}\,day^{-1}$	0.10
Nitrate half saturation constant	k_{NO_3}	$mmol\,N\,m^{-3}$	0.67
Phosphate half saturation constant	k_{PO_4}	$mmol\,P\,m^{-3}$	0.0015
Respiration rate	R_{phy,NO_3}	day^{-1}	0.05
Mortality rate	$M_{phy,det}$	day^{-1}	0.05
Maximum sinking speed	w_P	$m\,day^{-1}$	2.5
Coccolithophores (P_3)			
Maximum growth rate	$\mu_{phy,max}$	day^{-1}	1.15
Initial P-I slope	α_1	$(W\,m^{-2})^{-1}\,day^{-1}$	0.033
Nitrate half saturation constant	k_{NO_3}	$mmol\,N\,m^{-3}$	1.0
Phosphate half saturation constant	k_{PO_4}	$mmol\,P\,m^{-3}$	0.0015
Respiration rate	R_{phy,NO_3}	day^{-1}	0.05
Mortality rate	$M_{phy,det}$	day^{-1}	0.05
Maximum sinking speed	w_P	$m\,day^{-1}$	10.0

GMDD
4, 289–342, 2011

Table A2. Continued.

Parameter	Symbol	Units	Value
Diatoms (P_1)			
Zooplankton (Z)			
Maximum grazing rate	$\mu_{zoo,max}$	day^{-1}	1.2
Ingestion half saturation constant	k_{phy}	$(mmol\,N\,m^{-3})^{-2}$	0.25
Assimilation efficiency	γ		0.75
Excretion rate	E_{zoo,NO_3}	day^{-1}	0.1
Mortality rate	$M_{zoo,det}$	$day^{-1}(mmol\,N\,m^{-3})^{-1}$	0.1
Dissolved organic matter (DOM), detritus (det), and remineralization			
Remineralization rate of detritus	rem	day^{-1}	0.01
Remineralization rate of DON	k_{rn}	day^{-1}	0.00001
Remineralization rate of DOP	k_{rp}	day^{-1}	0.00001
Remineralization rate of DOSi	k_{rs}	day^{-1}	0.00001
Remineralization rate of DOC	k_{rc}	day^{-1}	0.0005
Fraction of dead phytoplankton converted to NH_4	a_p		0.8
Fraction of dead zooplankton converted to NH_4	a_z		0.8
Fraction of dead phytoplankton converted to DOM	a_p'		0.1
Fraction of dead zooplankton converted to DOM	a_z'		0.1
Maximum sinking speed	w_{det}	$m\,day^{-1}$	2.5
Ammonium (NH_4) nitrification			
Maximum rate of ammonium nitrification	$A_{n,max}$	$\mu mol\,m^{-3}\,day^{-1}$	0.02
Minimum light inhibition dosage for nitrification	D_{min}	$W\,m^{-2}$	0.0095
Half saturation dosage for nitrification photoinhibition	K_D	$W\,m^{-2}$	0.036
Calcite ($CaCO_3$)			
Maximum calcification to organic carbon production	R_{CaCO_3}		0.4
Calcite dissolution rate	γ_{CaCO_3}	day^{-1}	0.03
Chlorophyll-*a* (Chl-*a*)			
Minimum chlorophyll to nitrogen ratio	$Chl{:}N^{min}$	$mg\,Chl\,(mmol\,N)^{-1}$	1.5
Minimum chlorophyll to nitrogen ratio	$Chl{:}N^{max}$	$mg\,Chl\,(mmol\,N)^{-1}$	3.5
Critical irradiance for photoadaptation	I^*	$W\,m^{-2}$	25.0

GMDD
4, 289–342, 2011

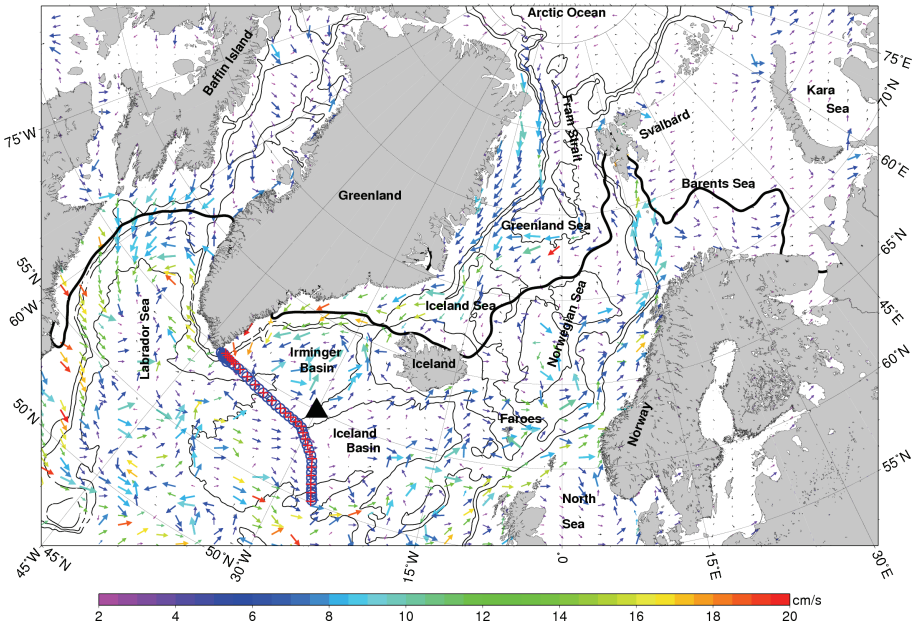

Fig. 1. Climatologic (1948–2009) annual surface currents derived from the 3-D ice-ocean model. The color bar indicates the current speed. The black thick line is the Arctic Front represented by the 4 °C isotherm and the thinner lines are the bathymetry contours (500, 1500, and 3000 m). The black triangle indicates the site chosen for the 1-D ecosystem-carbon model. The blue circles (1994) and red crosses (2004) indicate the location of the two repeat CARINA transects.

GMDD
4, 289–342, 2011

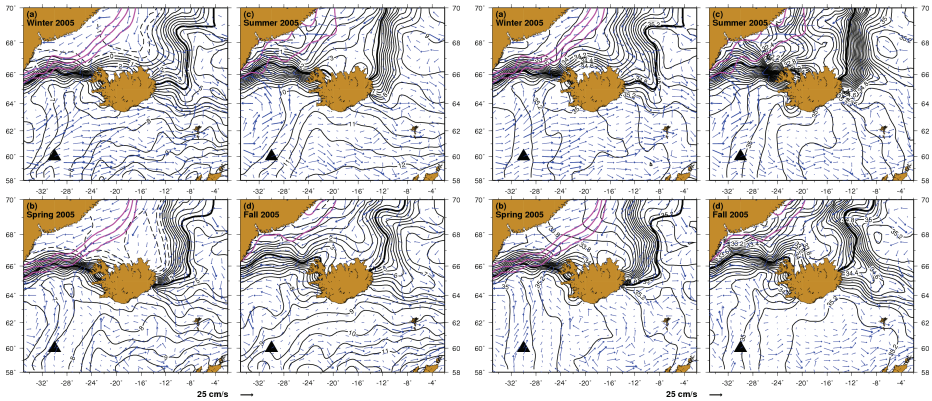

Fig. 2. Seasonal maps of MODIS Aqua SST (left panel, **a** through **d**) and 3-D model SSS (right panel, **a** through **d**) for 2005. The 3-D model surface currents (blue vectors) and ice concentration contours (20%, 40%, and 60% purple contours) derived from NOAA CDC are superposed. The 1-D model site is shown by the black triangle and the thick black lines indicate the Arctic Front.

GMDD
4, 289–342, 2011

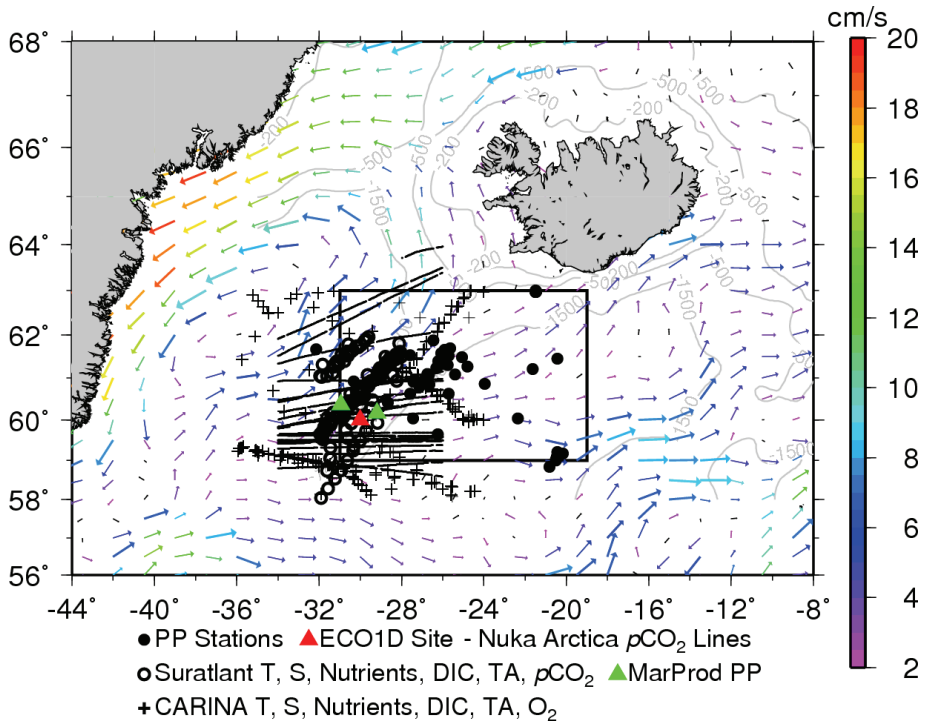

Fig. 3. Map showing the 3-D model annual climatologic surface currents, the location of the 1-D ecosystem model simulations, and PP, nutrients, and carbon in situ data used for model validation. The rectangular box bounds the CPR standard area B6 from which taxonomy data were obtained for validation.

GMDD
4, 289–342, 2011

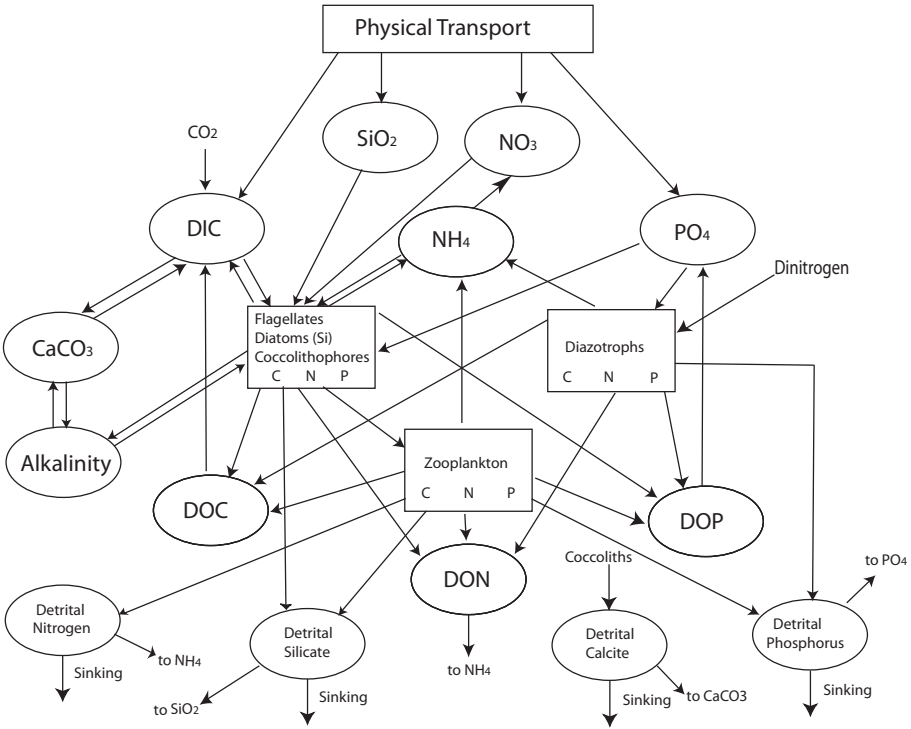

Fig. 4. Diagram of main components of the one-dimensional biogeochemical model.

GMDD
4, 289–342, 2011

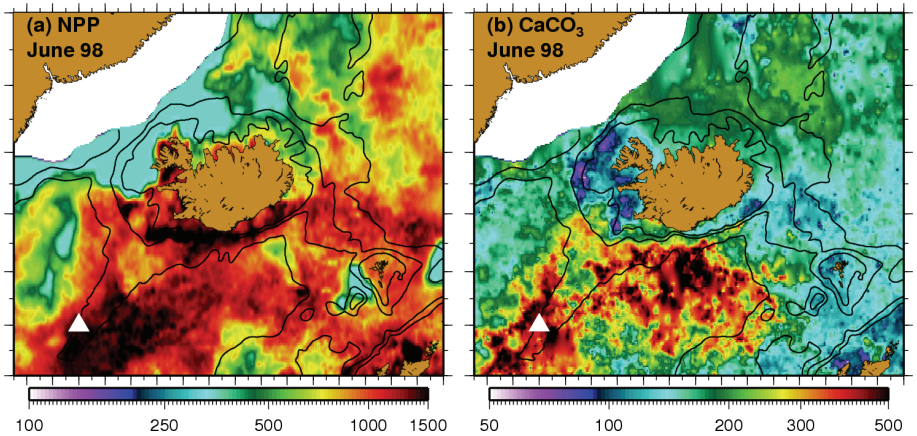

Fig. 5. Satellite-derived net primary production **(a)** and calcification rate **(b)** for June 1998 (units in mg C m^{-2} d^{-1}). The white triangle indicates the position of the 1-D ecosystem-carbon model simulations. Ice concentrations greater than 10% are masked in white.

GMDD
4, 289–342, 2011

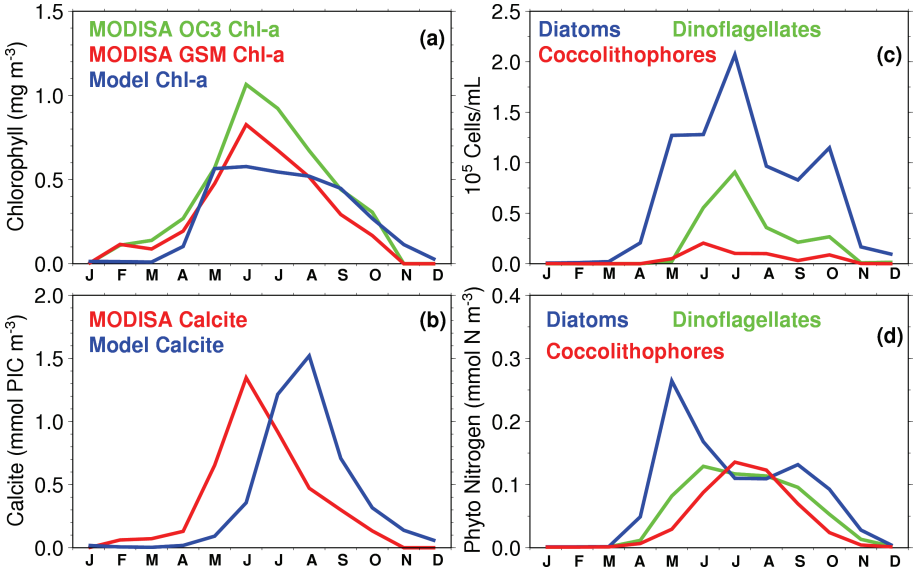

Fig. 6. Seasonal cycles of MODIS OC3 and GSM Chl-*a* with 1-D model Chl-*a* superposed **(a)**, MODIS and model calcite **(b)**, in situ CPR cell counts for diatoms, dinoflagellates, and coccolithophores **(c)**, and model nitrogen-based concentrations of diatoms, dinoflagellates, and coccolithophores **(d)**.

GMDD
4, 289–342, 2011

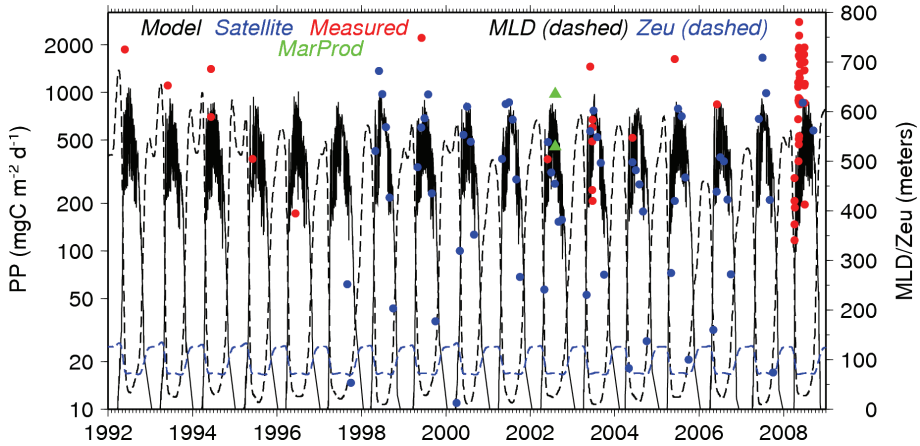

Fig. 7. Time series of 1-D model, satellite, and measured PP. Note that the productive phase of the bloom occurs when the MLD is equal to or shallower *Zeu*.

GMDD
4, 289–342, 2011

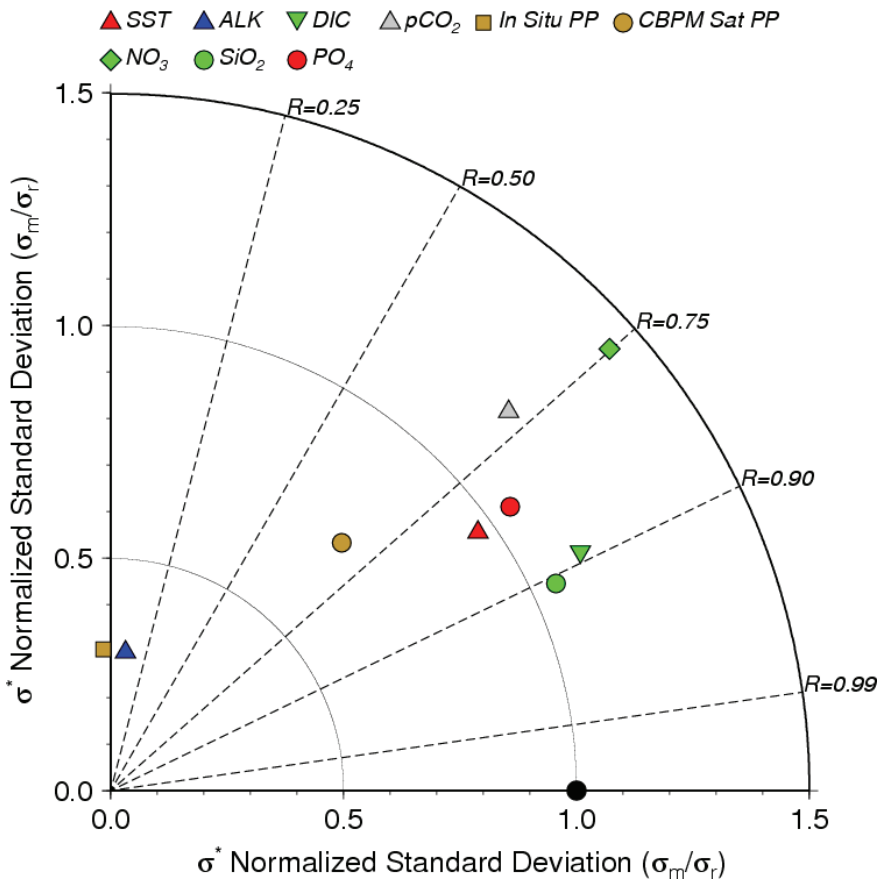

Fig. 8. Taylor diagram showing normalized standard deviations ($\sigma*$) and correlation coefficients (R) for model versus reference values consisting of all measured variables from different available sources. The black circle shows the result that would be obtained for a perfect fit between model and data, e.g., identical standard deviations and $R = 1$.

GMDD
4, 289–342, 2011

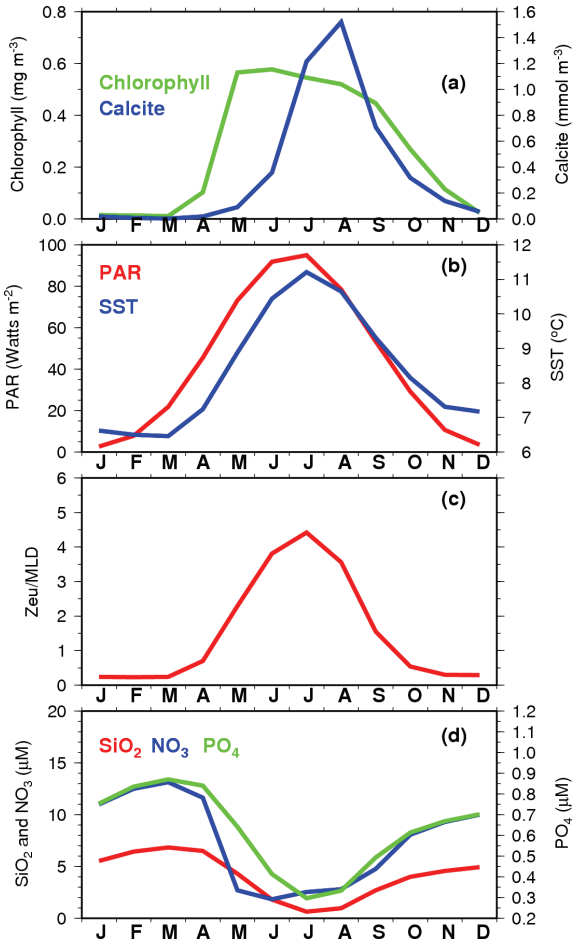

Fig. 9. Seasonal cycles of Chl-*a* and calcite **(a)**, PAR and SST **(b)**, Zeu:MLD ratio **(c)**, and nutrients **(d)**.

GMDD
4, 289–342, 2011

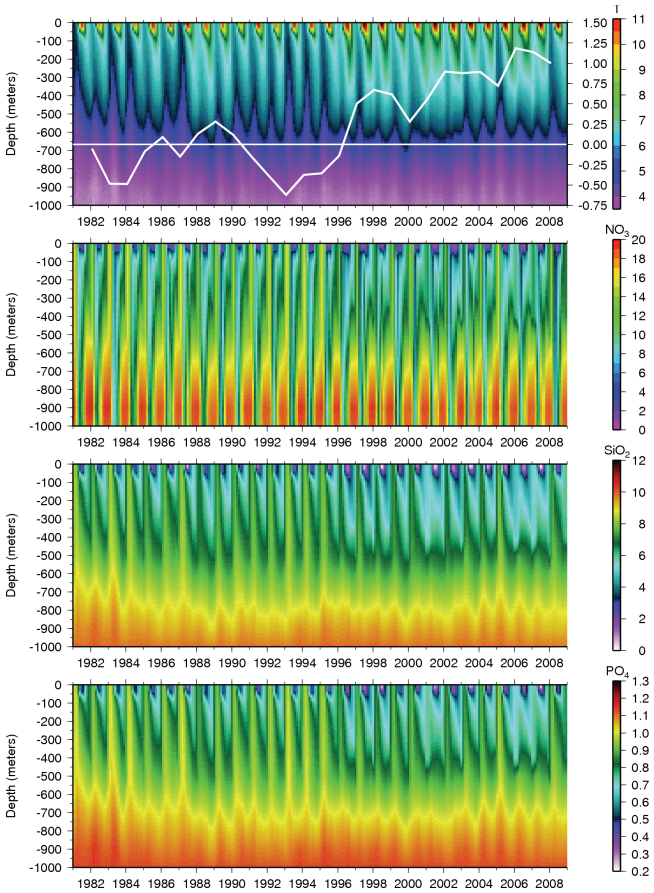

Fig. 10. Time series of model vertical profiles of temperature (°C), nitrate, silicate, and phosphate (μM) for the entire period of simulation (1981–2008). The white line superposed on the temperature panel is the winter (DJFM) SST anomaly.

GMDD
4, 289–342, 2011

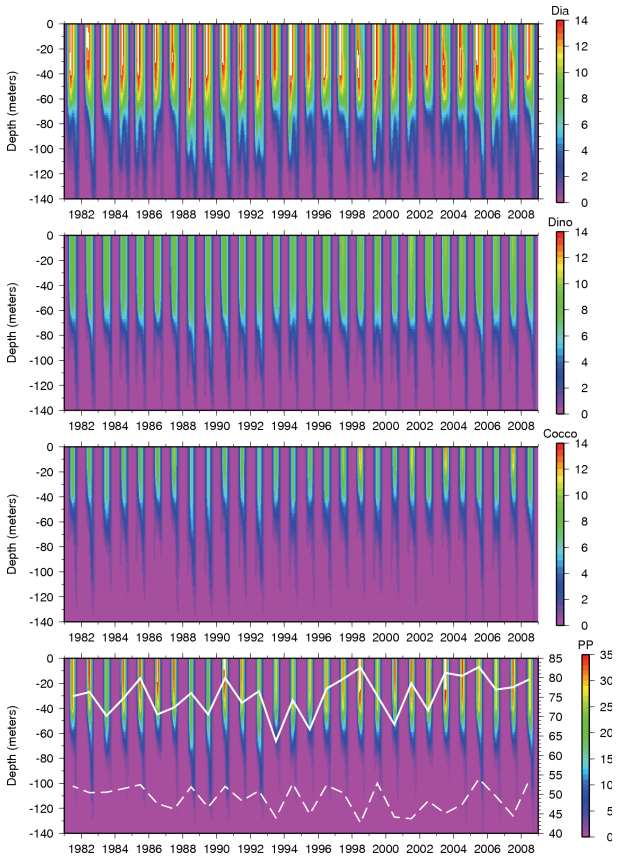

Fig. 11. Time series of model vertical profiles of diatoms, dinoflagellates, and coccolithophores biomass (mg C m^{-3}). The bottom panel shows the profiles of primary production (mg C m^{-3} d^{-1}). The superposed white lines are the annual vertically integrated primary production (solid) and the annual vertically integrated net community production (dashed) in units of g C m^{-2} yr^{-1}.

GMDD
4, 289–342, 2011

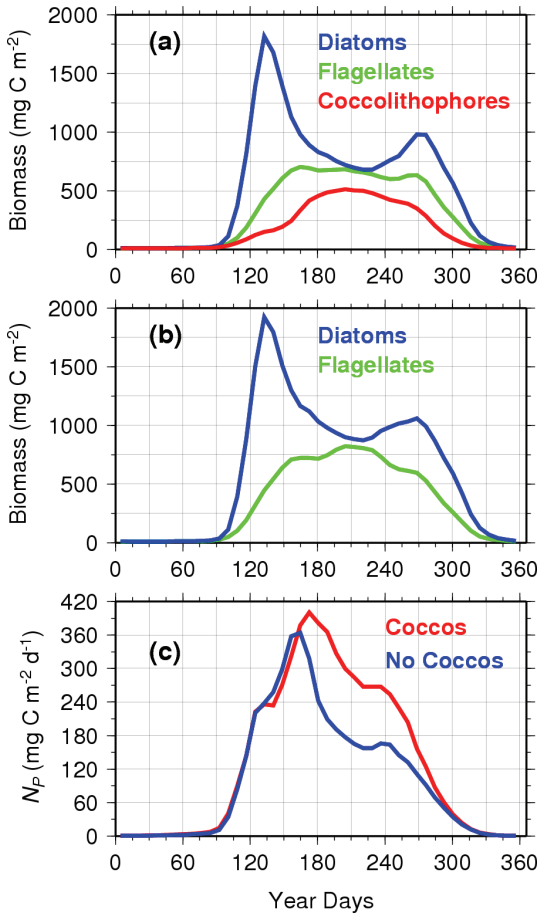

Fig. 12. Seasonal concentration of phytoplankton functional groups biomass with and without the presence of coccolithophores (**a** and **b**, respectively), and net community production with and without coccolithophores **(c)**.

GMDD
4, 289–342, 2011

The role of phytoplankton dynamics in the seasonal variability

S. R. Signorini et al.

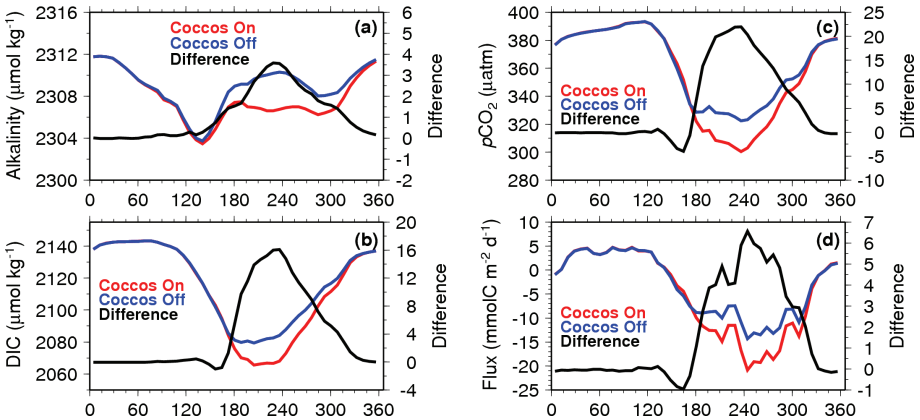

Fig. 13. Seasonal (1998–2008) changes of alkalinity **(a)**, DIC **(b)**, surface ocean pCO_2 **(c)**, and sea-air CO_2 flux **(d)** with (red) and without (blue) coccolithophores. The black line is the difference.

GMDD
4, 289–342, 2011